



Reconciling geochemical and geophysical observations of magma supply and melt distribution at the 9°N overlapping spreading center, East Pacific Rise

V. D. Wanless

Department of Geology and Geophysics, Woods Hole Oceanographic Institution, Woods Hole, Massachusetts 02540, USA (dwanless@whoi.edu)

M. R. Perfit

Department of Geological Sciences, University of Florida, Gainesville, Florida 32611, USA

E. M. Klein

Nicholas School of the Environment, Duke University, Durham, North Carolina 27708, USA

S. White

Department of Earth and Ocean Sciences, University of South Carolina, Columbia, South Carolina 29208, USA

W. I. Ridley

U.S. Geological Survey, Denver, Colorado 80225, USA

[1] Early studies of mid-ocean ridge discontinuities, such as transform faults and overlapping spreading centers, suggested a lower magma supply compared to ridge segment centers. This is reflected in bathymetrically deeper ridge axes, decreased hydrothermal activity, and the eruption of more evolved lava compositions. While many signatures of lower magma supply are observed at the 9°N overlapping spreading center on the East Pacific Rise, geophysical studies indicate extensive sub-surface melt in the region, suggesting that the present magmatic system is not diminished. Here major and trace element concentrations of erupted lavas are used to better understand magma supply at a large second-order ridge discontinuity. We show that the wide range of lava compositions erupted at the 9°N overlapping spreading center is generally consistent with early petrologic models of ridge propagation and require variable degrees of fractional crystallization, extensive magma mixing, and in some instances crustal assimilation. Moderately evolved ferrobasalts and FeTi basalts erupted at the OSC indicate that crustal residence times are long enough for significant crystallization of all magmas within the region, but the presence of dacitic lavas reflects periods of even lower magma supply, where melt replenishment is subordinate to cooling and crystallization. The geophysical observations of extensive melt within the shallow crust are reconciled with the geochemistry of the lavas, if melts are supplied intermittently to the propagating ridge over relatively short timescales.

Components: 14,200 words, 10 figures, 4 tables.

Keywords: East Pacific Rise; dacite; magma supply; melt lens; mid-ocean ridge; overlapping spreading center.

Index Terms: 1032 Geochemistry: Mid-oceanic ridge processes (3614, 8416); 3045 Marine Geology and Geophysics: Seafloor morphology, geology, and geophysics; 3618 Mineralogy and Petrology: Magma chamber processes (1036).

Received 27 March 2012; **Revised** 25 September 2012; **Accepted** 25 September 2012; **Published** 6 November 2012.

Wanless, V. D., M. R. Perfit, E. M. Klein, S. White, and W. I. Ridley (2012), Reconciling geochemical and geophysical observations of magma supply and melt distribution at the 9°N overlapping spreading center, East Pacific Rise, *Geochem. Geophys. Geosyst.*, 13, Q11005, doi:10.1029/2012GC004168.

1. Introduction

[2] An outstanding problem in mid-ocean ridge (MOR) geology lies in trying to reconcile geophysical and geochemical observations of magma supply at ridge discontinuities. On fast spreading ridges, increasing depths of ridge axes toward segment ends (near transform faults or overlapping spreading centers (OSC)) are thought reflect their magmatically starved nature compared to more robust segment centers [e.g., *Macdonald and Fox*, 1983; *Macdonald et al.*, 1988a]. Evidence of lower magma supply at ridge discontinuities also includes a decrease in high-temperature hydrothermal activity [e.g., *Haymon et al.*, 1991], a gradual shift from volcanically to tectonically dominant seafloor morphology [*White et al.*, 2002], and eruption of more evolved magma compositions [e.g., *Sinton et al.*, 1983, 1991]. For example, conventional models of ridge propagation, primarily based on geochemical data, hypothesize lower magma supply and cooler ocean crust (the ‘cold edge effect’) at segment ends compared to segment centers [e.g., *Christie and Sinton*, 1981]. This may result in the formation of more evolved lava compositions from greater degrees of fractional crystallization at the cold ridge tip [e.g., *Perfit and Fornari*, 1983; *Sinton et al.*, 1983]. While these characteristics of decreased magmatism have been well documented at several 1st and 2nd order discontinuities [*Macdonald and Fox*, 1983; *Sinton et al.*, 1983; *Macdonald et al.*, 1988b; *Smith et al.*, 2001], geophysical observations [*Detrick et al.*, 1987; *Harding et al.*, 1993; *Kent et al.*, 1993, 2000; *Bazin et al.*, 2001; *Tong et al.*, 2002; *Singh et al.*, 2006; *Toomey et al.*, 2007] at the well-studied 9°N OSC (Figure 1) appear to indicate extensive melt from the crust-mantle transition to the shallow melt lens, contradicting the paradigm of low magma supply at ridge segment ends.

[3] Seismic reflection and refraction studies at the 9°N OSC reveal a shallow melt lens beneath both limbs of the OSC (Figure 2), including one of the widest (~4 km) shallow-level melt bodies observed on any MOR [*Kent et al.*, 2000]. The wide melt

lens is located beneath the northernmost section of the eastern limb of the OSC and extends ~4 km west of the ridge axis [*Kent et al.*, 2000]. The wide melt lens narrows to <500 m in width and plunges ~600 m on-axis moving south as it approaches the southern tip where it eventually pinches out [*Kent et al.*, 2000]. The depth of the eastern melt lens varies from 1,650 to 2,200 m below the seafloor from north to south [*Singh et al.*, 2006]. Geophysical studies of the crust also reveal a significant amount of melt is stored within the crystal rich mid-to lower crustal regions [*Bazin et al.*, 2003] and compliance measurements indicate extensive melt in the lower crust [*Crawford and Webb*, 2002]. Tomographic studies of the OSC reveal a mantle low-velocity zone (MLVZ) at ~9 km depth near the mantle-crust transition, which has been interpreted as representing ~1–3% melt in the uppermost mantle [*Toomey et al.*, 2007]. Geophysical studies indicate thicker average seismic layer 2A within the overlap basin and at the propagating ridge tip [*Bazin et al.*, 2001; *Singh et al.*, 2006] but studies off-axis suggest that overall crustal thicknesses produced at the OSC through time are either similar to or thinner than average northern EPR crust [*Barth and Mutter*, 1996; *Canales et al.*, 2003]. These recent observations of shallow level melt lenses, melt in the lower crust, and a pronounced MLVZ in the upper mantle beneath the east limb may suggest that the current magmatic state of the OSC is relatively robust.

[4] In this study, we use geochemical evidence to evaluate magma supply and melt distribution at the 9°N OSC and try to reconcile our findings with previous geophysical studies of the region and traditional petrologic models of propagating ridges. We use major and trace element concentrations to address several questions relating to magma supply at the 9°N OSC, including: (1) What is the distribution of rock types at the OSC and can it be explained by classic models of ridge propagation? (2) What petrologic processes can account for the eruption of moderately to highly evolved basalts throughout the OSC? (3) Do the wide crustal melt lens and pronounced MLVZ beneath the region suggest that melt supply is elevated at the OSC?

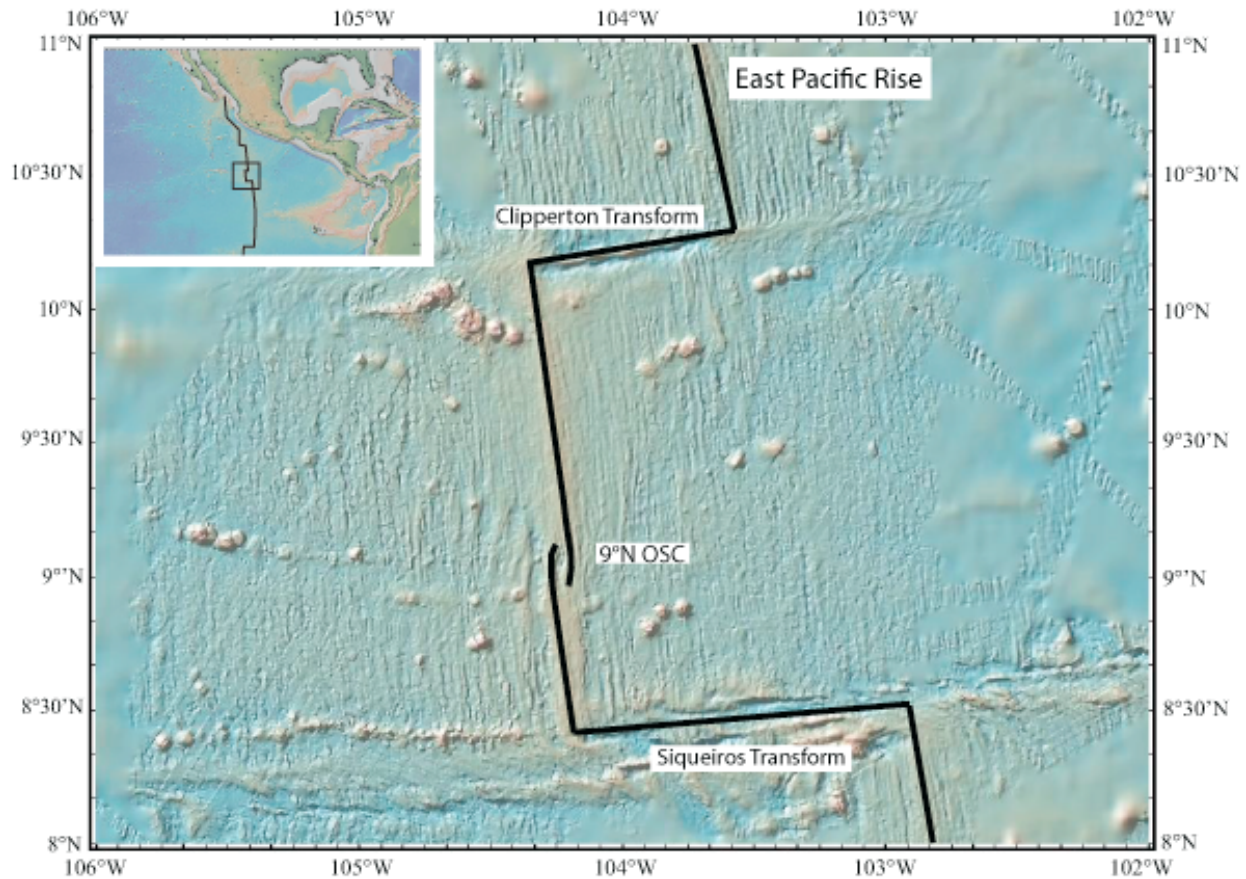


Figure 1. Bathymetric map highlighting the approximate location of the northern East Pacific Rise (black line). The location of the 9°N OSC is also shown. (Data from GeoMapApp [Carbotte *et al.*, 2004].)

(4) Can the geophysical observations be reconciled with the petrologic data at the OSC?

2. Background

2.1. Geologic Setting

[5] The 9°N OSC is located between the Clipperton and Siqueiros transform faults (Figure 1) and is one of eight 2nd order discontinuities on the northern EPR [Macdonald and Fox, 1983]. It consists of two north-south trending limbs that overlap by ~ 27 km and offset the ridge by up to ~ 8 km [Sempere and Macdonald, 1986]. The OSC can be divided into three main provinces: the eastern propagating limb, the western receding limb, and an overlap basin separating the two limbs (Figure 3). The eastern limb can be further subdivided into the east limb ridge, the east limb tip and the east limb flank region, following nomenclature in Nunnery *et al.* [2008]. Based on geologic, magnetic and bathymetric studies, the eastern limb has been propagating south at a rate of

~ 42 km/Myr, while overtaking the dying western limb [Macdonald and Fox, 1983; Carbotte and Macdonald, 1992]. The propagation of the east limb into cooler, variably altered crust is fundamental to the generation and eruption of high-silica andesites and dacites almost exclusively on this eastern limb of the OSC [Wanless *et al.*, 2010].

2.2. Petrologic Models of Propagating Ridges

[6] A detailed model describing the consequences of ridge propagation on lava compositions is presented by Christie and Sinton [1981] and Sinton *et al.* [1983]. This petrologic model suggests that the wide range of lava compositions erupted at ridge segment ends are related to both the thermal conditions of the crust and magma supply as the spreading rate decreases toward the ridge tip. Furthermore, their studies show that there are systematic variations in lava compositions moving back from the tip of the propagating ridge that are related

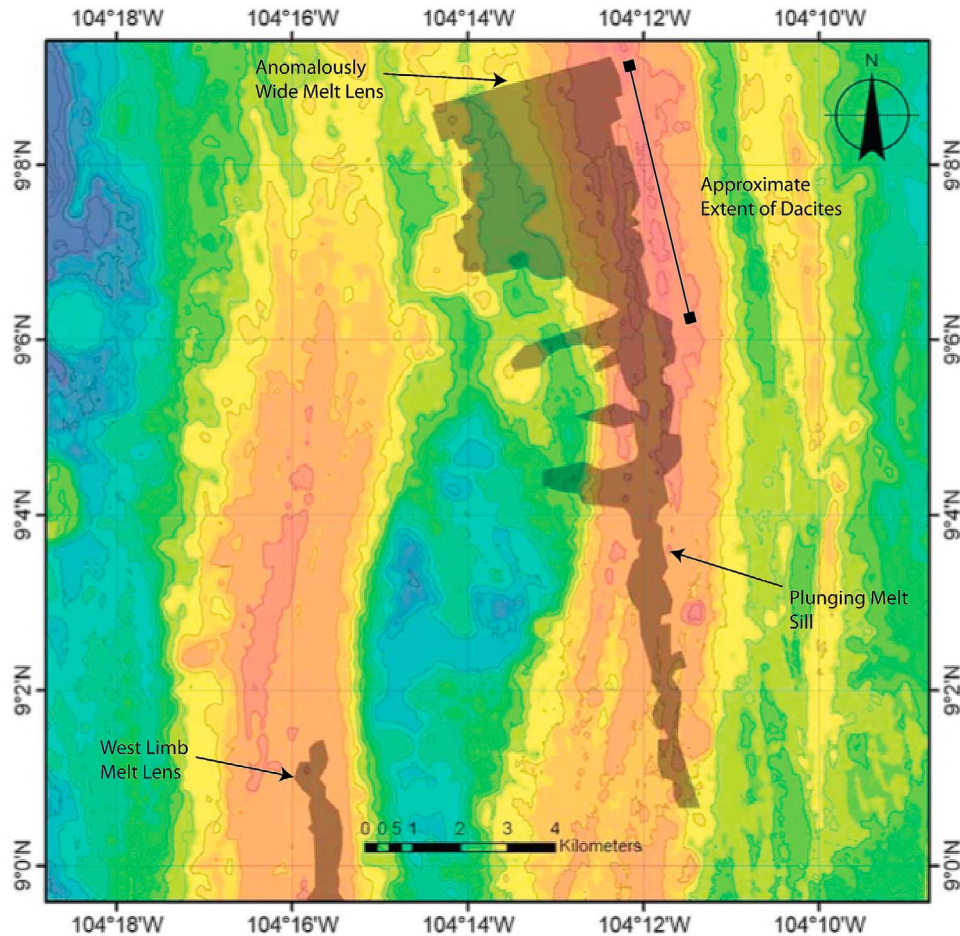


Figure 2. Bathymetric map of the 9°N OSC produced from combined SM2000 multibeam sonar and DSL-120A sonar phase bathymetry collected during the MEDUSA2007 cruise. The approximate location of the seismically imaged melt lens underlying the east and west limbs of the OSC is superimposed (gray shading) [Kent *et al.*, 2000]. Black bar represents the approximate extent of dacite eruptions.

to the balance between the cooling rate of melt bodies within the crust and magma supply from the mantle [e.g., Sinton *et al.*, 1983].

[7] In detail, the Christie and Sinton [1981] petrologic model of ridge propagation suggests that lavas erupted within ~ 3 km of the ridge tip should have high-MgO ($> \sim 8$ wt %), reflecting low crustal residence times (no melt lens) and limited fractional crystallization during ascent through the crust. Approximately 2–3 km behind the ridge tip, small discontinuous, melt bodies may form in the crust, increasing crustal residence times of melts and the extent of fractional crystallization, and thus, ferro- and FeTi basalts dominate the erupted lava compositions. With increasing distance from the ridge tip, crustal residence time, magma supply, and magma mixing will increase and erupted lava compositions may range from ferrobasalts to highly evolved andesites and dacites. The greatest

compositional variability is predicted to occur ~ 20 – 30 km behind the ridge tip. Beyond this point, increasing magma supply will result in a gradual transition into a steady state system, where extensive magma mixing and moderate degrees of fractional crystallization lead to the development of typical mid-ocean ridge basalts (MORB).

[8] The specific compositions erupted and distances over which these transitions occur will vary, due to differences in thermal structure controlled by factors including propagation rate, offset length, and spreading rate [e.g., Sinton *et al.*, 1983]. For example, not all propagating ridges are comprised of high-MgO lavas near their tips, and instead ridge tips can be dominated by moderately evolved ferro- and FeTi basalts [Perfit *et al.*, 1983; Smith *et al.*, 1994; Stakes *et al.*, 2006]. Unfortunately, the distance over which the greatest composition variability occurs is not well constrained because of the

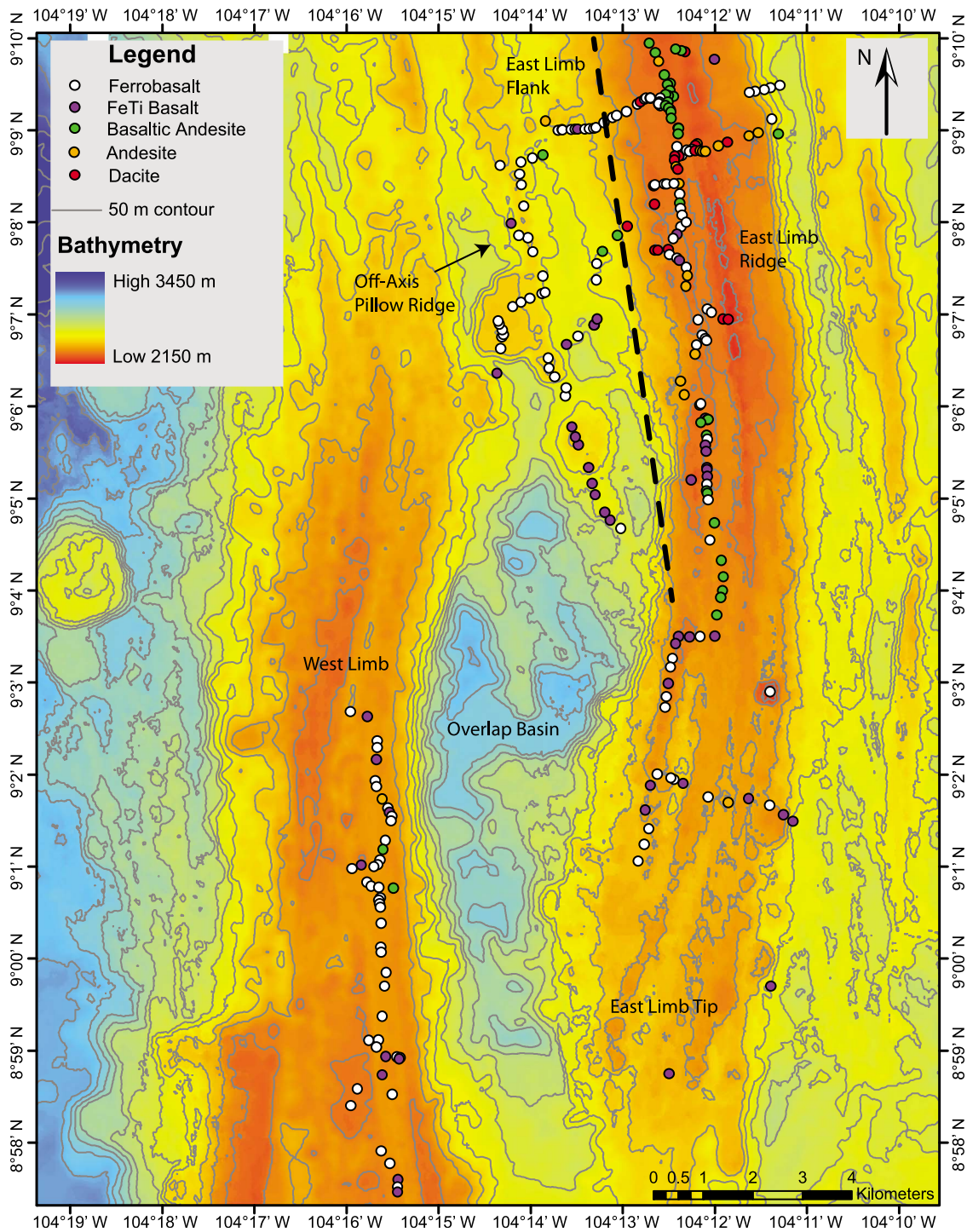


Figure 3. Bathymetric map of the 9°N OSC with contours at 50 m intervals (gray lines). Dashed line divides the east limb flank from the east limb axis. Circles show sample locations collected using the ROV *Jason2* during the *MEDUSA2007* cruise, with colors representing various rock types.

lack of detailed studies at propagating ridges, OSC and RTI. Therefore, when considering the effects of propagation on lava composition, each ridge discontinuity should be considered independently.

2.3. Generation of MOR High-Silica Lavas

[9] Below we present the petrologic results of the most thorough study of an OSC to date [see also *Langmuir et al., 1986; White et al., 2009; Wanless*

et al., 2010, 2011]. Compared to the normal, magmatically robust ridge segments to the north ($\sim 9^{\circ}30$ to 10° N [e.g., *Goss et al.*, 2010; *Perfit et al.*, 2012]), the OSC region is markedly different in the dominant presence of highly evolved (ferrobasalts and FeTi basalts) N-type MORB, andesites and dacites [*Langmuir et al.*, 1986; *Wanless et al.*, 2010, 2011]. Although the temporal relationships between these lava types and the presumed crustal-magmatic conditions at depth are unclear, the geochemistry of the eruptive rocks, particularly the high-silica varieties, can provide important constraints on how the magmatic system has operated in the past. First we briefly describe results from recent detailed studies of the petrogenesis of high-silica lavas at the OSC in order to better constrain the magmatic conditions necessary to produce the range of composition observed at the OSC.

[10] Recent petrologic studies have focused on the formation of high-silica lavas near segment ends [*Wanless et al.*, 2010, 2011]. At 9° N on the EPR, propagation of the east limb into cooler, altered crust is fundamental to the generation and eruption of high-silica andesites and dacites almost exclusively behind the tip of the propagating limb of the OSC [*Wanless et al.*, 2010]. These studies generally support the propagating ridge hypothesis, however, the MOR dacite compositions cannot be formed from extensive fractional crystallization alone. Instead, assimilation of altered ocean crust in combination with fractional crystallization (AFC) is required to explain elevated Cl, K_2O , and incompatible trace element concentrations [*Wanless et al.*, 2010] and relatively low oxygen isotope ratios [*Wanless et al.*, 2011]. Anomalous trace element concentrations and oxygen isotope ratios in andesites erupted along the propagating ridge on the eastern Galapagos Spreading Center also suggest crustal assimilation was important in magma evolution [*Perfit et al.*, 1999]. Assimilation of crustal material in any magmatic environment requires that there is enough latent heat of crystallization to melt the surrounding wall rock and thus, it appears that extensive crystallization of MORB are required at the 9° N OSC to produce the high-silica lavas by the combination of assimilation and fractional crystallization [*Wanless et al.*, 2010].

3. Analytical Methods

[11] A suite of 280 rock samples was collected from the 9° N OSC during the *MEDUSA2007* cruise (Figure 3). Of these, 275 have glassy outer rims, from which glass was handpicked, cleaned and

subsequently analyzed on a JOEL 8900 electron microprobe for major and minor element concentrations at the USGS facility in Denver, CO. Eight to ten points were analyzed per sample. The probe diameter was routinely $20\ \mu\text{m}$, to minimize sodium loss, with an accelerating voltage of 15 keV and a beam current of 20 nA. Natural and synthetic minerals were used as calibration standards and secondary normalizations involved the JdF-D2 (basalt glass [*Reynolds*, 1995]), ALV 2392–9 (UFL in-house basalt glass), and GSC (USGS dacitic glass standard) to account for instrumental drift [*Smith et al.*, 2001]. Chlorine concentrations, as well as high-precision potassium values, were also determined, using 200-s peak/100 s background counting times.

[12] A representative subset of fresh glasses was handpicked, cleaned in dilute acid, and dissolved for trace element and isotope analyses following methods described in *Goss et al.* [2010]. Seventy-three samples from the OSC were analyzed for high precision trace elements on a Thermo Element2 Inductively Coupled Plasma Mass Spectrometer (ICP-MS) at the University of Florida (UF). External calibration was done to quantify results using a combination of internal UF (ENDV – Endeavor and ALV 2392–9) and USGS (AGV-1, BIR-1, BHVO-1, BCR-2 and STM-1) rock standards. High precision Pb, Sr, and Nd isotopic abundances on 37 samples were determined using the Nu Instruments Plasma multicollector ICP-MS at UF [*Wanless et al.*, 2010]. Detailed descriptions of sample preparation, dissolution procedures, standards, and statistical data are given in *Goss et al.* [2010] and *Kamenov et al.* [2008].

4. Geochemical Results

[13] Here we report major and trace element data from both limbs of the OSC (Tables 1–4). Overall, samples from the east limb include basalts (ferrobasalts and FeTi basalts), basaltic andesites, andesites and dacites; no high-MgO basalts (e.g., maximum MgO = 7.36 wt. % on the east limb) were recovered from this region. Radiogenic isotope ratios and dacitic major and trace element compositions are presented in *Wanless et al.* [2010] and volatile element contents and oxygen isotope ratios are presented in *Wanless et al.* [2011]; representative dacitic compositions are presented in Tables 1 and 2 for comparison.

4.1. Basalts

[14] Basalts are defined here as lavas with 49–52 wt% SiO_2 (Table 1). In comparison to the dominantly

Table 1 (Sample). East Limb Major Element Data 9°N OSC [The full Table 1 is available in the HTML version of this article]

Sample	Rock Type	SiO ₂	TiO ₂	Al ₂ O ₃	FeOt	MnO	MgO	CaO	Na ₂ O	K ₂ O	P ₂ O ₅	Cl
WC-07	FeTi	49.3	2.60	12.6	14.1	0.24	5.71	9.2	3.21	0.20	0.28	
WC-06	FeTi	49.7	2.49	12.7	14.0	0.24	5.67	9.3	3.28	0.19	0.27	
WC-08	ferrobasalt	50.0	1.75	13.8	11.1	0.21	7.27	10.9	2.90	0.15	0.16	
WC-01	ferrobasalt	50.1	1.83	13.7	11.4	0.21	7.20	10.9	2.94	0.14	0.18	
265-43	ferrobasalt	50.5	1.92	13.9	11.6	0.21	6.98	11.1	2.86	0.13	0.19	0.01
WC-02	ferrobasalt	50.1	1.80	13.7	11.3	0.21	7.26	11.0	2.94	0.13	0.20	
265-98	ferrobasalt	50.2	1.94	13.8	11.7	0.21	7.17	10.9	2.86	0.12	0.19	
266-14	ferrobasalt	50.4	2.14	13.5	12.4	0.22	6.69	10.7	3.11	0.16	0.22	
264-08	FeTi	50.1	2.68	12.7	14.1	0.26	5.69	9.6	3.27	0.21	0.28	0.07
266-15	ferrobasalt	50.5	2.38	13.1	13.3	0.23	6.27	10.1	3.27	0.18	0.26	
266-51	ferrobasalt	50.6	1.94	13.9	11.6	0.21	7.33	11.0	2.86	0.13	0.19	0.01
267-14	ferrobasalt	50.6	1.92	14.0	11.6	0.21	6.96	11.1	2.86	0.13	0.21	
265-20	ferrobasalt	50.7	1.85	13.9	11.3	0.22	7.21	11.3	2.95	0.13	0.18	0.01
266-48	ferrobasalt	50.6	1.92	14.1	11.6	0.21	7.34	11.0	3.03	0.13	0.19	
266-38	FeTi	50.6	2.00	13.6	12.3	0.23	6.63	10.7	3.15	0.17	0.20	
267-13	ferrobasalt	50.6	1.85	14.1	11.3	0.21	7.11	11.2	2.82	0.12	0.21	
267-03	FeTi	50.6	2.13	13.6	12.5	0.23	6.45	10.2	3.05	0.16	0.26	
264-23	ferrobasalt	50.6	1.87	13.9	11.3	0.22	7.28	11.1	2.92	0.13	0.18	
266-16	ferrobasalt	50.6	2.02	13.7	12.1	0.23	6.87	10.7	3.15	0.16	0.22	
265-44	ferrobasalt	50.6	1.93	14.0	11.7	0.22	6.86	11.1	2.81	0.13	0.19	
266-40	ferrobasalt	50.6	1.77	14.0	11.5	0.20	7.24	11.3	2.96	0.14	0.16	
266-17	ferrobasalt	50.6	1.87	14.0	11.3	0.20	7.24	11.4	3.01	0.14	0.19	
265-99	ferrobasalt	50.6	1.84	13.9	11.4	0.20	7.36	11.0	2.90	0.13	0.18	
266-34	ferrobasalt	50.6	1.84	14.1	11.3	0.21	7.25	11.1	2.90	0.11	0.18	
265-87	ferrobasalt	50.7	1.98	13.8	11.9	0.23	6.84	11.1	2.77	0.14	0.20	
266-32	ferrobasalt	50.7	1.85	14.0	11.4	0.22	7.27	11.1	2.92	0.12	0.18	
265-96	ferrobasalt	50.7	1.83	14.0	11.4	0.19	7.35	11.0	2.85	0.13	0.18	
267-05	FeTi	50.7	1.99	13.7	12.0	0.22	6.39	10.3	3.06	0.16	0.25	
264-05	ferrobasalt	50.7	1.83	13.8	11.4	0.22	7.07	11.1	2.95	0.15	0.18	
267-12	FeTi	50.7	2.20	13.6	12.7	0.22	6.38	10.4	3.03	0.16	0.25	
266-39	FeTi	50.7	2.04	13.6	12.4	0.24	6.57	10.5	3.21	0.19	0.20	
267-08	FeTi	50.7	1.99	13.8	12.0	0.21	6.79	10.8	2.95	0.14	0.22	
265-19	ferrobasalt	50.6	1.83	14.0	11.2	0.21	7.19	11.2	2.93	0.12	0.18	0.01
266-33	ferrobasalt	50.7	1.84	14.0	11.4	0.22	7.29	11.1	2.88	0.12	0.20	
266-13	ferrobasalt	50.7	2.29	13.2	12.9	0.23	6.34	10.5	3.21	0.17	0.25	
266-52	ferrobasalt	50.7	1.93	13.9	11.6	0.21	7.30	11.0	2.89	0.13	0.18	
265-14	ferrobasalt	50.8	1.83	13.9	11.2	0.21	7.16	11.2	2.97	0.12	0.18	
WC-05	ferrobasalt	50.8	2.00	13.4	11.5	0.21	6.11	9.7	3.35	0.26	0.27	
266-02	FeTi	50.8	2.08	13.6	12.4	0.22	6.68	10.5	3.11	0.12	0.21	
266-08	ferrobasalt	50.8	1.98	13.9	11.7	0.22	7.12	10.9	2.86	0.13	0.20	
265-86	ferrobasalt	50.8	1.99	13.8	11.9	0.22	6.79	11.1	2.72	0.14	0.20	
267-09	ferrobasalt	50.8	1.95	13.9	12.0	0.22	6.90	10.8	2.95	0.14	0.24	
265-97	ferrobasalt	50.8	2.02	13.8	12.0	0.22	7.03	10.9	2.61	0.13	0.21	
265-82	ferrobasalt	50.8	1.95	13.8	11.7	0.22	6.93	11.2	2.69	0.14	0.19	0.01
265-92	ferrobasalt	50.8	1.98	13.9	11.8	0.22	7.08	11.0	2.93	0.13	0.20	
265-10	ferrobasalt	50.8	1.86	13.9	11.3	0.22	7.13	11.2	2.99	0.13	0.18	
265-52	ferrobasalt	50.8	1.93	14.0	11.8	0.22	6.99	11.2	2.92	0.13	0.20	
265-15	ferrobasalt	50.8	1.86	13.9	11.3	0.21	7.14	11.2	2.99	0.13	0.17	
267-11	FeTi	50.8	2.20	13.7	12.7	0.22	6.44	10.3	2.95	0.16	0.25	
266-19	ferrobasalt	50.8	1.86	13.7	11.9	0.23	6.88	11.0	3.09	0.14	0.20	
266-12	ferrobasalt	50.8	2.15	13.4	12.7	0.24	6.51	10.7	3.27	0.18	0.22	
265-68	ferrobasalt	50.8	1.81	14.0	11.2	0.21	7.29	11.5	2.79	0.13	0.17	0.01
265-53	ferrobasalt	50.8	1.96	14.0	11.8	0.22	6.85	11.2	2.92	0.13	0.19	
266-18	ferrobasalt	50.8	2.01	13.7	12.1	0.22	6.91	10.9	3.14	0.16	0.22	
266-37	FeTi	50.8	2.03	13.6	12.3	0.22	6.73	10.6	3.02	0.15	0.20	
265-62	ferrobasalt	50.8	1.95	13.9	11.7	0.22	6.92	11.2	2.90	0.13	0.19	
266-11	ferrobasalt	50.8	2.23	13.3	12.9	0.24	6.43	10.3	3.26	0.18	0.27	
267-07	ferrobasalt	50.8	1.96	13.9	11.8	0.20	6.96	10.9	2.94	0.14	0.22	
265-13	ferrobasalt	50.8	1.85	14.0	11.2	0.22	7.21	11.3	2.93	0.12	0.18	
265-11	ferrobasalt	50.8	1.80	14.0	11.1	0.21	7.23	11.3	2.95	0.12	0.17	

Table 2. Trace Element Data 9°N OSC

	Sample																			
	265-43	264-08	266-33	267-09	265-88	265-72	266-22	265-18	264-04	266-28	266-07	265-78	267-15	266-01	266-10	265-35	265-31	265-113	265-24	
Li	7.8	10.0	7.5	8.2	8.0	7.7	8.2	7.5	8.5	9.2	7.7	7.8	7.9	6.0	8.5	7.8	7.9	11.0	15.3	
Sc	42	42	41	42	41	42	43	43	53	40	36	43	41	33	46	42	42	38	27	
V	347	450	321	354	351	350	359	338	406	357	337	353	330	273	347	342	342	323	196	
Cr	109	18	155	87	69	96	50	166	120	41	9	84	139	41	150	127	112	32	12	
Co	41	43	40	41	42	42	43	42	51	41	38	43	40	34	44	41	41	39	27	
Ni	54	34	48	46	47	54	38	53	72	32	47	52	51	38	57	57	54	34	16	
Cu	59	60	61	60	60	60	61	64	76	55	50	64	58	51	65	62	59	51	31	
Zn	94	116	88	96	97	96	99	95	103	100	93	95	93	79	99	96	94	103	118	
Ga	18	21	18	19	18	18	19	18	24	20	17	18	18	14	21	18	18	21	23	
Rb	1.1	2.1	1.2	1.5	1.2	1.1	1.0	1.0	1.6	1.5	1.5	1.2	1.4	1.0	1.5	1.2	1.2	2.2	4.7	
Sr	119.9	126.4	113.6	113.4	123.6	117.2	119.8	126.2	146.4	111.3	98.0	124.8	107.6	88.8	121.5	119.3	118.4	111.1	99.4	
Y	43.8	58.9	39.1	43.6	44.3	43.9	45.2	41.9	45.4	43.0	42.1	43.3	42.4	31.6	46.9	44.5	44.4	61.0	94.5	
Zr	126	180	125	140	133	126	130	122	142	157	139	124	136	95	156	130	131	229	468	
Nb	3.08	5.46	2.91	3.65	3.46	3.07	3.03	2.76	4.01	3.87	3.84	3.19	3.42	2.20	3.87	3.15	3.21	5.67	10.33	
Cs	0.01	0.03	0.02	0.02	0.01	0.01	0.01	0.01	0.02	0.02	0.02	0.02	0.02	0.02	0.02	0.02	0.02	0.03	0.06	
Ba	8.37	17.07	8.25	11.12	10.31	8.44	7.85	6.87	13.20	10.35	11.73	9.49	9.99	6.46	11.08	8.69	8.75	15.60	29.41	
La	4.54	6.81	4.13	4.79	4.94	4.47	4.61	4.27	4.98	5.40	4.84	4.64	4.50	3.10	5.17	4.66	4.71	7.63	14.86	
Ce	14.16	20.51	13.18	14.97	14.97	13.90	14.38	13.40	15.49	17.22	14.95	14.06	14.13	9.93	16.46	14.43	14.56	23.69	45.03	
Pr	2.34	3.32	2.29	2.56	2.46	2.31	2.38	2.21	2.61	2.95	2.47	2.31	2.44	1.76	2.77	2.38	2.40	3.92	7.01	
Nd	12.6	17.3	12.1	13.5	13.2	12.5	12.8	11.9	13.9	15.5	13.1	12.5	13.0	9.5	14.7	12.7	12.7	20.1	35.1	
Sm	4.42	5.99	4.16	4.69	4.48	4.37	4.45	4.15	4.78	5.48	4.49	4.35	4.47	3.32	5.00	4.47	4.44	6.68	10.74	
Eu	1.48	1.94	1.45	1.58	1.52	1.46	1.52	1.40	1.67	1.77	1.49	1.47	1.49	1.18	1.66	1.48	1.48	1.99	2.75	
Gd	5.78	7.74	5.53	6.10	5.92	5.75	5.87	5.46	6.18	7.03	5.78	5.71	5.82	4.42	6.40	5.82	5.83	8.52	12.94	
Tb	1.08	1.45	1.02	1.14	1.11	1.07	1.11	1.02	1.15	1.30	1.07	1.07	1.07	0.82	1.19	1.10	1.09	1.58	2.36	
Dy	7.22	9.69	6.62	7.36	7.32	7.09	7.31	6.74	7.46	8.41	6.92	7.04	7.04	5.34	7.71	7.24	7.24	10.13	15.14	
Ho	1.52	2.05	1.43	1.56	1.53	1.51	1.55	1.44	1.57	1.82	1.46	1.49	1.50	1.14	1.61	1.54	1.54	2.20	3.19	
Er	4.39	5.94	4.04	4.47	4.48	4.34	4.51	4.15	4.55	5.18	4.27	4.33	4.27	3.26	4.68	4.44	4.45	6.26	9.36	
Tm	0.67	0.91	0.62	0.68	0.68	0.66	0.69	0.63	0.68	0.80	0.64	0.66	0.66	0.50	0.70	0.68	0.68	0.96	1.44	
Yb	4.43	6.01	3.97	4.35	4.47	4.33	4.55	4.16	4.41	5.15	4.17	4.37	4.19	3.19	4.55	4.45	4.45	6.17	9.27	
Lu	0.68	0.93	0.60	0.66	0.68	0.67	0.70	0.64	0.68	0.76	0.63	0.66	0.64	0.48	0.70	0.69	0.68	0.95	1.42	
Hf	3.44	4.83	3.20	3.58	3.59	3.40	3.50	3.23	3.59	4.04	3.49	3.37	3.46	2.50	3.90	3.54	3.52	5.72	11.27	
Ta	0.21	0.37	0.20	0.25	0.23	0.21	0.21	0.19	0.28	0.26	0.27	0.22	0.22	0.16	0.27	0.21	0.22	0.36	1.50	
Pb	0.39	0.61	0.60	0.59	0.45	0.40	0.41	0.38	0.59	0.87	0.58	0.42	0.77	0.42	0.68	0.46	0.42	0.95	1.63	
Th	0.18	0.34	0.18	0.23	0.20	0.18	0.18	0.16	0.22	0.25	0.23	0.20	0.21	0.13	0.22	0.19	0.20	0.40	0.84	
U	0.08	0.13	0.08	0.09	0.08	0.07	0.07	0.07	0.09	0.10	0.09	0.08	0.08	0.06	0.09	0.08	0.08	0.15	0.31	

Table 2. (continued)

	Sample																			
	265-50	265-125	265-109	264-16	265-57	265-103	265-91	265-90	265-100	266-05	265-69	265-25	264-14	266-56	265-66	264-09	265-70	265-42	265-83	265-95
Li	28.9	14.3	19.2	18.5	20.7	22.3	23.6	28.2	27.1	20.4	26.3	28.1	26.4	27.4	36.9	26.7	33.6	31.6	32.4	31.4
Sc	13	31	29	33	31	26	25	24	24	26	22	19	24	17	26	12	12	14	11	10
V	73	247	176	230	217	129	93	70	100	216	180	87	160	93	184	46	45	58	32	52
Cr	4	50	29	44	32	6	2	5	10	10	16	9	41	5	15	4	4	3	3	3
Co	13	31	27	30	29	23	21	20	21	26	21	17	21	15	23	10	10	11	8	8
Ni	7	29	23	25	18	10	6	6	10	15	11	9	22	7	15	6	5	6	5	5
Cu	20	46	35	34	27	27	23	22	26	33	22	26	29	22	24	16	16	15	14	15
Zn	100	97	126	129	137	144	147	174	150	107	112	124	114	106	143	89	106	119	103	98
Ga	29	23	27	24	26	30	31	30	33	26	28	28	26	29	42	28	29	30	29	30
Rb	12.5	4.2	4.4	4.6	5.3	5.3	5.7	6.3	6.5	7.0	7.3	10.8	7.8	10.7	11.6	12.9	15.0	13.7	15.5	12.5
Sr	69.1	96.3	103.8	112.6	109.0	103.0	105.8	114.3	112.2	91.5	87.7	96.8	97.5	81.3	114.0	77.7	78.0	82.8	76.2	61.0
Y	138.0	71.6	110.4	101.2	115.9	135.2	144.1	170.0	152.5	104.7	113.9	154.4	123.7	132.8	164.0	150.9	160.0	160.1	159.1	144.9
Zr	967	380	557	371	425	671	724	680	721	645	605	881	542	901	945	824	934	816	922	985
Nb	14.82	6.33	10.95	8.89	10.06	13.51	14.52	15.81	16.24	10.90	11.39	17.36	11.40	15.17	16.79	14.89	15.90	16.36	15.57	16.53
Cs	0.12	0.05	0.05	0.05	0.07	0.06	0.06	0.08	0.07	0.08	0.08	0.14	0.10	0.11	0.12	0.13	0.17	0.16	0.17	0.13
Ba	58.22	24.31	28.72	29.81	32.73	33.81	36.06	42.35	41.77	38.30	40.22	58.57	43.51	53.60	62.57	65.65	72.69	70.01	76.40	62.17
La	28.00	11.10	15.75	13.61	15.76	19.57	21.43	23.72	23.67	17.91	18.93	28.81	19.39	25.36	28.95	28.98	30.89	29.03	30.69	29.16
Ce	79.99	32.73	48.54	41.17	47.56	60.43	66.14	73.19	72.67	52.40	55.75	84.42	56.99	73.59	84.22	83.89	88.15	82.95	87.16	83.65
Pr	11.64	5.08	7.76	6.42	7.34	9.64	10.54	11.55	11.30	7.89	8.40	12.25	8.47	10.86	12.53	11.97	12.49	11.98	12.32	12.02
Nd	52.4	24.6	38.9	30.9	35.3	48.6	52.9	55.8	56.3	37.2	39.7	54.9	39.1	49.6	58.3	52.7	55.0	53.5	54.0	54.6
Sm	15.64	7.54	12.07	10.37	11.90	14.99	16.18	18.61	17.27	11.43	12.26	16.73	12.38	14.91	17.07	15.92	16.67	16.69	16.46	15.64
Eu	2.96	1.98	3.15	2.68	2.98	3.78	4.10	4.57	4.20	2.60	2.81	3.31	2.75	3.07	3.78	2.95	3.09	3.39	3.05	2.89
Gd	17.82	9.21	14.75	12.89	14.65	18.33	19.83	22.78	20.71	13.66	14.69	19.55	14.82	17.58	20.38	18.54	19.47	19.69	18.90	17.66
Tb	3.41	1.72	2.70	2.44	2.78	3.34	3.57	4.26	3.79	2.53	2.76	3.68	2.86	3.25	3.83	3.55	3.69	3.76	3.64	3.35
Dy	22.37	11.31	17.61	16.19	18.52	21.76	23.38	27.74	24.73	16.76	18.27	24.22	19.28	21.34	25.32	23.80	25.06	25.37	24.51	22.13
Ho	4.79	2.39	3.71	3.44	3.93	4.52	4.89	5.88	5.24	3.60	3.98	5.17	4.14	4.60	5.42	5.12	5.38	5.47	5.27	4.74
Er	14.29	7.09	10.97	10.16	11.60	13.34	14.24	17.37	15.41	10.63	11.66	15.49	12.44	13.59	16.36	15.66	16.42	16.48	16.18	14.61
Tm	2.30	1.12	1.69	1.58	1.81	2.05	2.20	2.68	2.38	1.68	1.86	2.49	1.98	2.18	2.58	2.52	2.63	2.64	2.62	2.32
Yb	15.29	7.23	10.88	10.43	11.91	13.19	14.01	17.70	15.34	10.90	12.12	16.50	13.15	14.05	16.83	16.84	17.54	17.56	17.54	15.12
Lu	2.29	1.10	1.66	1.62	1.84	2.07	2.14	2.73	2.36	1.67	1.85	2.64	2.04	2.16	2.55	2.61	2.73	2.75	2.72	2.32
Hf	23.87	9.42	13.27	10.10	11.55	15.95	17.25	17.78	17.09	15.73	15.48	22.31	14.75	21.69	23.08	22.68	24.80	22.24	24.75	24.51
Ta	0.89	0.45	0.76	0.61	0.68	0.95	1.03	1.03	1.14	0.66	0.69	1.13	0.80	0.91	1.23	1.04	1.10	1.12	1.08	1.23
Pb	3.54	1.73	2.55	1.65	1.89	3.28	3.76	2.41	3.08	2.02	2.96	3.07	2.67	3.21	6.24	2.76	3.84	3.47	3.80	4.12
Th	2.53	0.74	0.78	0.76	0.88	0.96	1.05	1.15	1.17	1.31	1.35	2.31	1.28	2.08	2.00	2.59	2.68	2.36	2.80	2.36
U	0.84	0.28	0.30	0.30	0.35	0.36	0.39	0.46	0.45	0.46	0.46	0.89	0.51	0.70	0.71	0.98	1.04	0.91	1.05	0.86

Table 3. West Limb Major Element Data 9°N OSC

Sample	Rock Type	SiO ₂	TiO ₂	Al ₂ O ₃	FeO	MnO	MgO	CaO	Na ₂ O	K ₂ O	P ₂ O ₅	Total
267-16	ferrobasalt	50.8	1.18	14.8	9.6	0.19	8.72	12.5	2.06	0.07	0.13	100.05
267-17	FeTi	51.1	2.12	13.5	12.2	0.22	6.74	10.7	2.98	0.11	0.23	99.89
267-18	ferrobasalt	51.1	1.71	14.3	10.6	0.18	7.70	11.2	2.70	0.10	0.17	99.81
267-19	ferrobasalt	51.0	1.83	14.0	11.1	0.20	7.40	10.9	2.78	0.10	0.20	99.53
267-20	FeTi	50.8	2.16	13.5	12.4	0.22	6.66	10.5	2.93	0.12	0.23	99.44
267-21	ferrobasalt	51.2	1.72	14.3	10.6	0.20	7.77	11.1	2.74	0.10	0.18	99.97
267-22	ferrobasalt	51.0	1.80	14.2	10.9	0.20	7.52	10.9	2.84	0.11	0.21	99.57
267-23	basaltic andesite	56.0	2.04	13.0	12.0	0.21	2.84	6.6	3.70	0.67	0.73	97.73
267-24	ferrobasalt	50.7	1.81	14.0	10.8	0.21	7.64	10.9	3.00	0.12	0.21	99.32
267-25	FeTi	50.9	2.06	13.5	12.4	0.23	7.29	10.8	2.59	0.15	0.24	100.20
267-26	ferrobasalt	50.7	1.86	13.7	11.6	0.22	7.21	10.8	2.87	0.16	0.22	99.31
267-27	ferrobasalt	50.7	1.87	13.4	11.4	0.22	7.12	10.6	2.82	0.17	0.25	98.61
267-29	ferrobasalt	51.7	1.61	13.6	11.2	0.21	7.00	10.5	2.80	0.22	0.19	98.97
267-30	basaltic andesite	52.3	1.92	13.3	12.1	0.23	5.43	9.1	3.25	0.37	0.48	98.45
267-32	ferrobasalt	50.6	1.75	14.0	10.6	0.20	7.76	10.9	2.99	0.12	0.20	99.14
267-33	ferrobasalt	50.7	1.78	14.0	10.7	0.20	7.71	10.9	2.99	0.12	0.21	99.39
267-34	ferrobasalt	50.7	1.80	14.0	10.7	0.21	7.73	10.9	2.98	0.12	0.18	99.25
267-35	FeTi	50.5	2.10	13.7	12.0	0.23	6.88	10.8	3.19	0.14	0.22	99.81
267-37	ferrobasalt	50.8	1.88	13.8	11.6	0.21	7.26	11.0	2.90	0.14	0.21	99.78
267-38	ferrobasalt	50.8	1.58	14.3	10.2	0.19	7.67	11.8	2.98	0.08	0.14	99.73
267-39	ferrobasalt	50.8	1.78	14.0	10.8	0.20	7.75	11.1	3.00	0.12	0.20	99.72
267-40	ferrobasalt	50.9	1.76	14.2	10.8	0.21	7.82	10.9	3.00	0.12	0.21	99.83
267-41	basaltic andesite	52.4	3.06	12.7	14.1	0.24	4.21	7.8	3.77	0.64	0.46	99.41
267-42	ferrobasalt	50.7	1.76	14.1	10.7	0.20	7.81	11.0	3.02	0.12	0.20	99.64
267-43	ferrobasalt	50.7	1.76	14.2	10.8	0.20	7.77	11.0	3.03	0.12	0.17	99.70
267-44	ferrobasalt	50.9	1.76	14.1	10.9	0.21	7.54	11.1	2.99	0.12	0.19	99.74
267-45	ferrobasalt	50.8	1.76	13.9	10.8	0.20	7.71	11.0	2.95	0.12	0.19	99.44
267-46	ferrobasalt	50.8	1.78	14.0	10.9	0.20	7.63	11.0	2.98	0.12	0.21	99.63
267-47	ferrobasalt	50.3	1.83	14.1	10.2	0.20	7.28	11.4	2.89	0.32	0.27	98.87
267-48	ferrobasalt	49.9	1.65	14.4	10.7	0.21	8.01	11.7	2.62	0.09	0.21	99.54
267-50	ferrobasalt	49.8	1.58	14.8	10.6	0.20	8.31	11.7	2.63	0.09	0.17	99.82
267-51	ferrobasalt	50.6	1.80	14.1	10.9	0.20	7.55	11.1	2.96	0.12	0.21	99.54
267-52	ferrobasalt	50.2	1.95	13.7	11.6	0.21	7.08	11.0	3.12	0.12	0.22	99.23
267-53	ferrobasalt	50.7	1.57	14.3	10.2	0.20	7.84	11.8	2.73	0.11	0.17	99.58
267-54	ferrobasalt	50.0	1.71	14.2	10.7	0.20	7.65	11.5	2.91	0.11	0.18	99.13
267-55	ferrobasalt	50.3	1.54	14.5	10.0	0.20	7.98	11.8	2.71	0.11	0.17	99.33
267-56	FeTi	50.2	2.22	13.0	13.1	0.24	6.42	10.1	3.09	0.15	0.26	98.78
267-57	ferrobasalt	49.8	1.36	14.9	9.3	0.18	8.35	12.4	2.55	0.14	0.16	99.20
267-58	ferrobasalt	50.0	1.82	14.3	10.2	0.21	7.22	11.5	2.88	0.32	0.27	98.70
267-59	FeTi	49.7	2.00	14.3	10.6	0.20	6.99	11.2	3.10	0.36	0.26	98.67
267-60	FeTi	50.1	2.12	13.1	12.5	0.23	6.73	10.4	2.97	0.14	0.24	98.61
267-61	ferrobasalt	49.5	1.56	14.8	10.5	0.20	8.17	11.6	2.62	0.09	0.18	99.20
267-62	ferrobasalt	50.7	1.35	14.6	9.4	0.18	8.34	12.0	2.46	0.08	0.14	99.30
267-63	ferrobasalt	50.1	1.43	14.0	9.9	0.20	8.10	12.1	2.41	0.09	0.16	98.47
267-64	ferrobasalt	49.7	2.40	14.7	10.8	0.19	6.46	10.2	3.19	0.59	0.41	98.59
267-65	ferrobasalt	51.0	1.72	14.0	10.9	0.21	7.50	11.1	2.66	0.12	0.18	99.33
267-66	ferrobasalt	49.9	2.11	13.3	12.3	0.22	6.76	10.2	2.87	0.13	0.23	97.99
267-67	FeTi	50.7	2.05	13.4	12.0	0.23	6.87	10.3	2.91	0.12	0.21	98.84
267-68	ferrobasalt	50.7	2.02	13.6	11.9	0.21	6.95	10.3	2.86	0.12	0.22	98.89
267-69	FeTi	50.8	2.04	13.5	12.0	0.21	6.97	10.3	2.88	0.12	0.21	99.14

“normal” mafic basalts from the heavily sampled 9°30′N–10°N segment of the northern EPR [e.g., *Langmuir et al.*, 1986; *Batiza and Niu*, 1992; *Perfit et al.*, 1994, 2012], those from the east limb of the OSC are primarily evolved ferrobasalts and FeTi basalts [>2 wt% TiO₂ and 12 wt% total iron as Fe²⁺ (FeOt)], with MgO concentrations ranging from 6.16 to 7.36 wt%, and high FeOt (10.83 to 13.50 wt%)

and TiO₂ (1.70 to 2.83 wt%) contents (Figures 4 and 5). All basaltic lavas on the east limb have chemical characteristics indicative of normal mid-ocean ridge basalt (N-MORB) with low K₂O (0.11 to 0.27 wt%), P₂O₅ (0.12 to 0.27 wt%) and Cl concentrations (0.004 to 0.05 wt%) that exhibit inverse correlations with MgO contents (Figure 5). K/Ti ratios (K₂O/TiO₂ × 100) are low, ranging from

Table 4. West Limb Trace Element Data 9°N OSC

	Sample							
	267-16	267-18	267-23	267-62	267-63	267-64	267-68	267-69
Li	5.3	6.9	19.4	5.4	5.6	7.9	8.2	7.7
Sc	40	41	26	40	39	41	42	41
V	275	312	148	278	266	345	368	350
Cr	368	147	24	359	339	240	80	71
Co	43	40	21	40	38	43	43	42
Ni	117	64	15	72	66	113	48	47
Cu	146	64	27	78	73	66	56	56
Zn	73	86	117	75	73	96	100	96
Ga	15	17	25	15	15	25	19	19
Rb	0.5	1.0	8.9	0.9	1.0	11.1	1.0	1.1
Sr	87.5	109.0	102.5	95.9	96.1	327.0	116.5	106.4
Y	26.6	36.7	126.7	28.8	28.9	42.8	47.3	43.4
Zr	62	112	669	82	82	208	133	134
Nb	1.55	2.48	19.92	2.00	2.16	21.36	3.22	3.13
Cs	0.01	0.02	0.11	0.01	0.02	0.12	0.01	0.02
Ba	3.39	7.24	70.75	7.07	7.31	131.32	8.56	9.24
La	2.38	3.65	23.42	2.86	2.90	15.43	4.80	4.52
Ce	7.21	11.68	66.80	8.95	9.02	36.58	14.93	14.46
Pr	1.21	2.08	10.13	1.54	1.59	4.96	2.47	2.47
Nd	6.98	11.05	48.44	8.39	8.63	22.53	13.42	13.23
Sm	2.44	3.86	14.98	2.95	3.03	5.96	4.72	4.58
Eu	0.89	1.34	3.55	1.07	1.11	2.00	1.60	1.55
Gd	3.37	5.08	18.03	3.93	4.07	6.87	6.15	5.89
Tb	0.65	0.93	3.28	0.73	0.75	1.17	1.16	1.10
Dy	4.26	6.08	21.11	4.74	4.90	7.27	7.67	7.14
Ho	0.93	1.30	4.50	1.01	1.06	1.48	1.61	1.50
Er	2.68	3.69	12.96	2.90	2.99	4.18	4.68	4.36
Tm	0.41	0.56	2.02	0.44	0.46	0.62	0.71	0.66
Yb	2.68	3.60	12.92	2.83	2.93	3.93	4.68	4.23
Lu	0.41	0.55	1.98	0.43	0.44	0.60	0.72	0.65
Hf	1.74	2.86	16.00	2.09	2.17	4.70	3.56	3.41
Ta	0.10	0.17	1.11	0.14	0.15	1.37	0.22	0.22
Pb	0.13	0.52	2.02	0.24	0.41	1.86	0.44	0.39
Th	0.09	0.15	1.85	0.12	0.14	1.42	0.18	0.18
U	0.04	0.06	0.54	0.05	0.06	0.42	0.07	0.07

6 to 13. Incompatible trace element concentrations are relatively high in these basalts compared to typical N-MORB from the northern EPR because of their more evolved nature. However, incompatible trace element ratios are relatively constant (Figure 6), despite eruption over a wide geographic region at the OSC and are comparable to other N-MORB erupted on the EPR. Rare earth element (REE) concentrations are remarkably similar in the ferrobasalts and FeTi basalts, with an average La_N/Yb_N ratio of 0.77 ± 0.05 and high field strength element (HFSE) ratios are also relatively constant with Zr/Nb of 40 ± 2.8 (Figure 6). Additionally, average Th/U ratios are 2.5 ± 0.2 and average Ba/Zr ratios are 0.08 ± 0.06 . Compatible trace element concentrations in the ferrobasalts and FeTi basalts vary greatly (Cr = 9 to 166 ppm; Ni = 32 to 71 ppm), but show steep decreasing trends with increasing Zr (Figure 7).

4.2. Basaltic Andesites and Andesites

[15] Basaltic andesites are defined as having 52 to <57 wt% SiO_2 and andesites as having 57 to <63 wt% SiO_2 (Table 1). These lavas are collectively referred to as intermediate composition lavas, as most of their elemental abundances are intermediate between the basalts and high-silica dacites. MgO concentrations in these lavas range from 1.5 to 6.5 wt% and FeOt ranges from 8.64 to 14.13 wt% (Figure 4). Minor elements are highly variable (Figure 5; P_2O_5 = 0.18 to 0.78 wt%; K_2O = 0.25 to 0.99 wt%; and Cl = 0.04 to 0.51 wt%), with most but not all samples showing inverse correlations between these elements and MgO. REE and HFSE concentrations exhibit quite large ranges, but have relatively constant ratios with average La_N/Yb_N ratios = 1.08 ± 0.12 and Zr/Nb = 47 ± 8.3 (Figure 6). Additionally, average Th/U ratios are

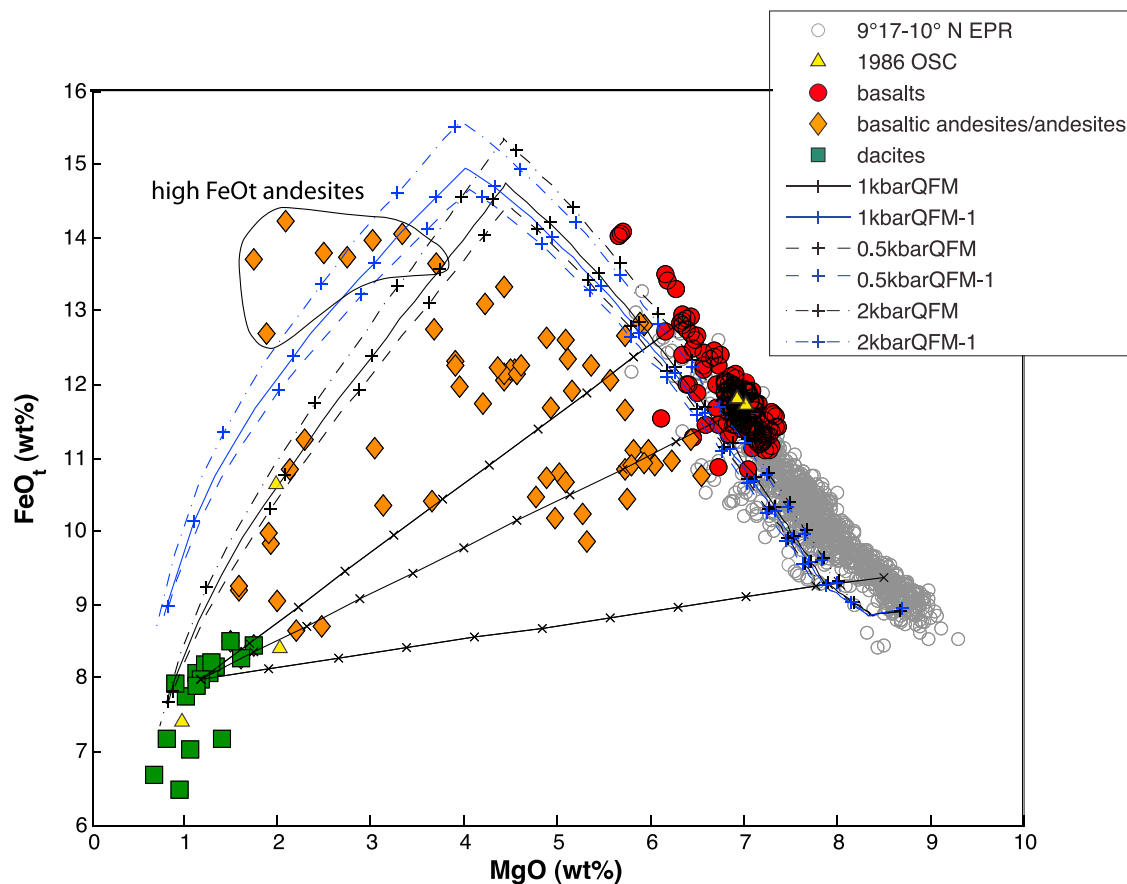


Figure 4. Total iron (FeOt) versus MgO concentrations of glasses collected from the east limb of the 9°N OSC. Compositions include basalts (red filled circles), intermediate compositions basaltic andesites and andesites (orange filled diamonds) and dacites (green filled squares). Lavas collected at the OSC from an earlier dredging cruise (dredge 82 on the east limb) are shown as yellow triangles [Langmuir *et al.*, 1986]. Lavas collected from the northern EPR (~9°17'N to 10°N) are shown as comparison (gray circles) and are generally more mafic compared to the OSC basalts (data from Perfit *et al.* [1994], Smith *et al.* [2001], Goss *et al.* [2010], and Perfit *et al.* [2012]). Errors are smaller than the symbol size. Liquid lines of descent are calculated using Petrolog [Danyushevsky and Plechov, 2011] at three different pressures and using oxygen fugacities of QFM and QFM-1 are superimposed. Pluses indicate 5% fractional crystallization. Solid black lines show binary mixing trends between a high-silica dacite and three different basaltic compositions, including a ferrobasalt and a FeTi basalt from the OSC and sample 2392–9 from the 1991 eruption at 9°50'N [Smith *et al.*, 2001]. Crosses represent 10% mixing intervals.

2.7 ± 0.17 and average Ba/Zr ratios are 0.07 ± 0.01 . Ni and Cr concentrations, ranging from 6 to 29 ppm and 2 to 50 ppm, respectively (Figure 7), are generally though not exclusively lower than in the ferrobasalts and FeTi basalts.

4.3. Dacites

[16] The geochemistry of the MOR dacites (>57 wt% SiO₂) are discussed in detail by Wanless *et al.* [2010, 2011], and five representative dacitic samples are shown in Tables 1 and 2. The dacites have SiO₂ concentrations as high as 67.5 wt% and MgO as low as 0.67 wt%. P₂O₅ concentrations range from 0.15 to 0.25 wt% (Figure 5). K₂O and Cl

concentrations average 1.17 and 0.63 wt% respectively. Highly incompatible trace element concentrations are elevated compared to those in the basalts and intermediate composition lavas. The dacites have average La_N/Yb_N ratios of 1.26 ± 0.10 , Zr/Nb of 58 ± 4.5 (Figure 6), Th/U of 2.7 ± 0.13 and Ba/Zr of 0.07 ± 0.01 .

5. Lava Petrogenesis at the OSC

5.1. On-Axis Basaltic Lavas

[17] No moderate to high-MgO (>8 wt. %) lavas were sampled anywhere along the east limb of the OSC (Figure 8), including the east limb ridge tip

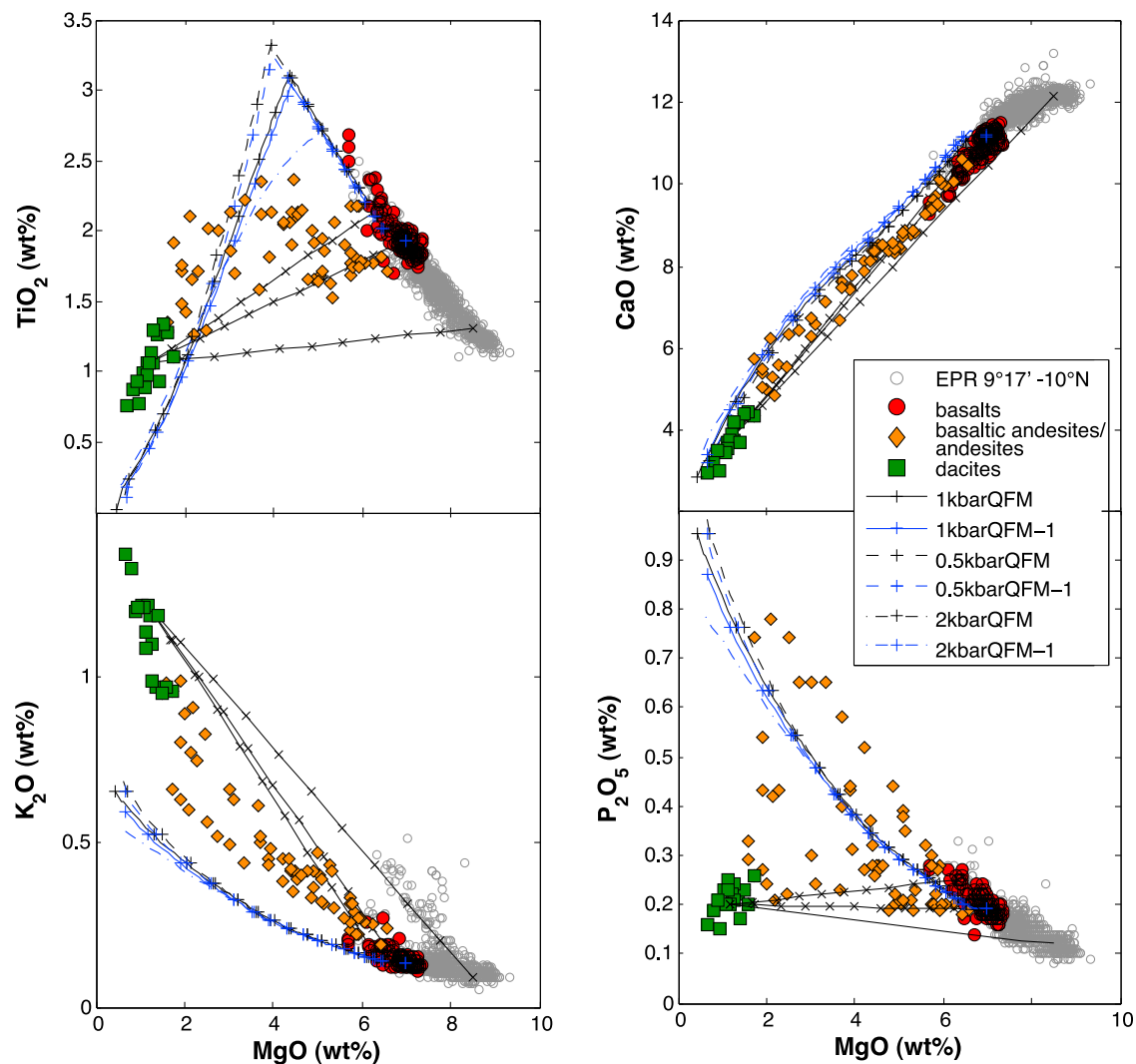


Figure 5. Major elements variations versus MgO for glasses collected from the east limb of the 9°N OSC. Symbols for the OSC basalts are the same as Figure 4. The lavas collected from the northern EPR (~9°17'–10°N) are generally more primitive compared to the OSC basalts. Liquid lines of descent calculated using Petrolog [Danyushevsky and Plechov, 2011] at three different pressures using oxygen fugacities of QFM and QFM-1 and a OSC basalt as a parent composition are shown with pluses indicating 5% crystallization intervals. Solid lines with black crosses show calculated bulk mixing lines between a high-silica dacite and three different basaltic compositions (see Figure 4). Note that mixing between more primitive basalts (compositionally similar to lavas from the northern EPR) and dacites cannot explain the variations observed in the intermediate lavas. Analytical errors are smaller than individual symbols.

(south of 9°04'N). Instead, east limb basalts are, on average, more evolved than typical N-MORB erupted along the northern EPR [Batiza and Niu, 1992; Perfit et al., 1994; Smith et al., 2001; Goss et al., 2010; Perfit et al., 2012]. The average east limb basalt contains 6.90 wt% MgO (median of 6.96 wt%) and the highest concentration of MgO measured is 7.36 wt% (Figures 4 and 5), which is slightly greater than the average of 7.26 wt% for the entire 8°–10°N ridge segment [Rubin and Sinton, 2007]. However, the average MgO concentration of ~1418 lavas from

the northern second-order segment of the EPR (9°15'N to ~10°N) is 7.87 ± 0.55 wt% (median of 7.80 wt%) with a maximum of 9.3 wt% MgO. There is a general trend toward lower average MgO contents (Figure 9) moving south and north of the 9°50'N eruption site [Batiza and Niu, 1992; Goss et al., 2010; Perfit et al., 2012]. Calculations using Petrolog [Danyushevsky and Plechov, 2011] suggest that major element compositions of ferrobasalts and FeTi basalts erupted on the east limb can be generated respectively by ~30% and ~55%

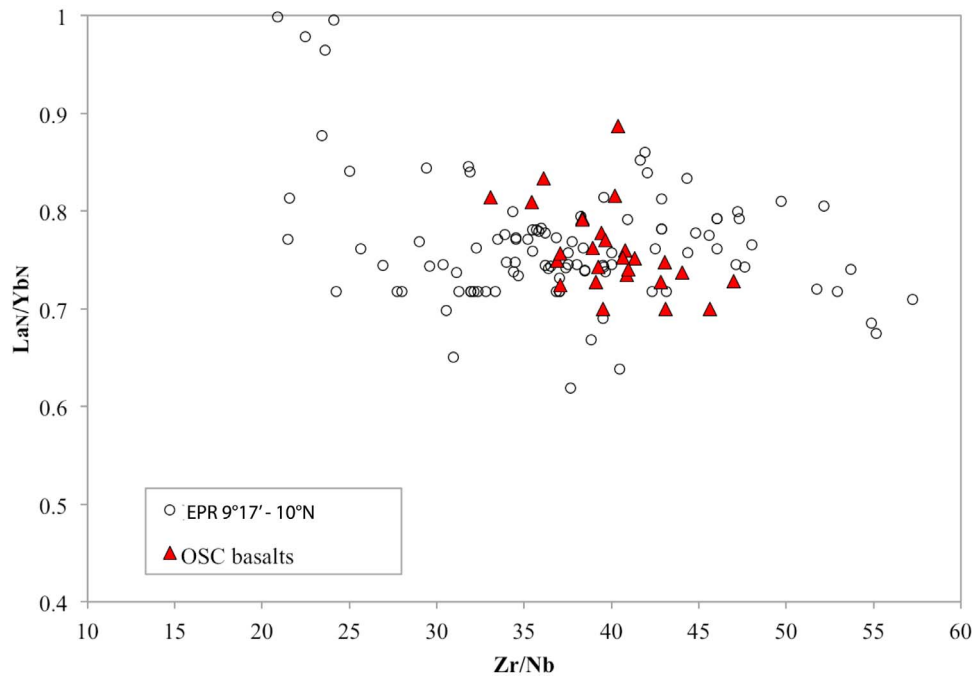


Figure 6. Trace element ratios for lavas erupted at the East Limb of the 9°N OSC. La_N/Yb_N and Zr/Nb ratios from the OSC basalts are similar to EPR N-MORB basalts from 9°17'–10°N [Perfit *et al.*, 1994, 2012]. The relatively low La_N/Yb_N ratios suggest that higher degrees of melting cannot account for the presence of a wide melt lens at the OSC.

fractional crystallization of ol + plag + cpx ($fO_2 =$ QFM; pressures of 1 to 2 kbar and $H_2O = 0.15$ wt %) from a relatively high-MgO (8.72 wt%), N-MORB parent basalt from the northern EPR (Figures 4 and 5). Slight deviations from calculated fractional crystallization trends likely represent variability in parental magma compositions, mixing of basalts

with different lineages or with more evolved lavas (andesites and dacites), and/or assimilation of small volumes of surrounding wall rock. MELTS [Ghiorso and Sack, 1995] calculations provided similar overall crystallization trends in major element data (particularly at low MgO concentrations), but did not reproduce the ferrobasalt and FeTi basalt

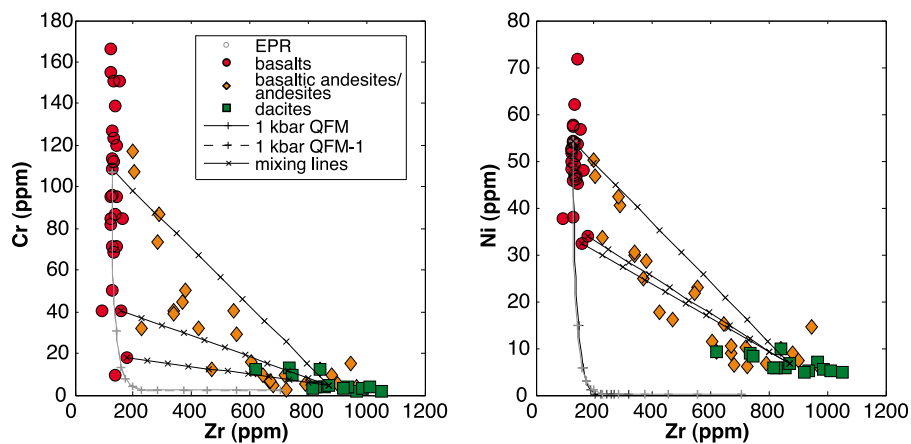


Figure 7. Compatible trace elements (Cr and Ni) versus MgO for glasses collected from the east limb of the 9°N OSC. Symbols and lines are the same as Figure 4. Liquid lines of descent calculated using Petrolog [Danyushevsky and Plechov, 2011] from a moderately evolved OSC basalt (265–43). Errors are smaller than the symbol size.

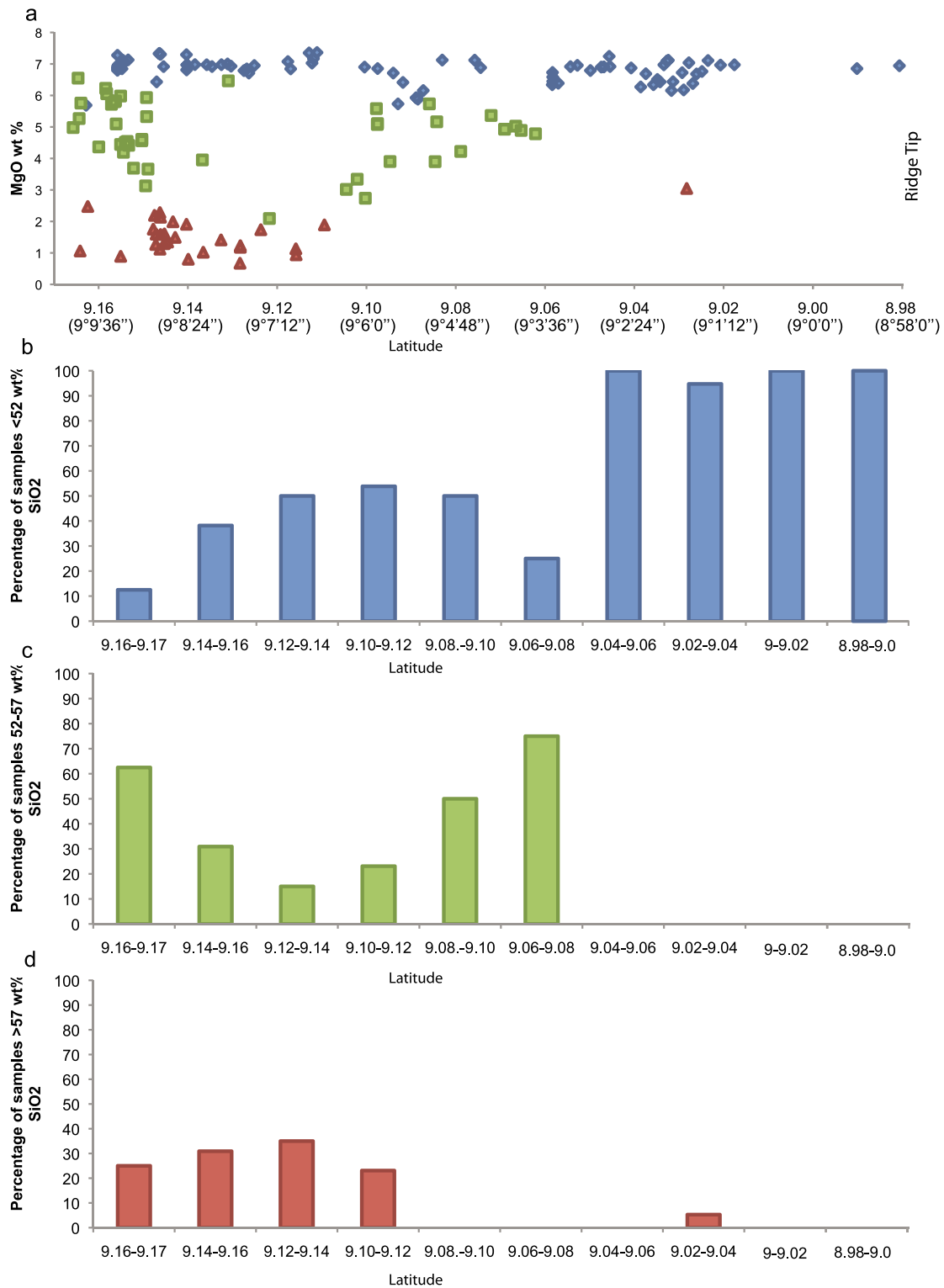


Figure 8. Diagram showing along-axis variations in lava compositions at the OSC. Samples included in the diagram were primarily collected on-axis between 104°12'W and 104°13'W and no samples from the east limb flank region or west limb are included. (a) MgO versus Latitude for all samples collected from the East Limb of the OSC. Basaltic compositions are found along the entire limb; however, MgO concentrations generally increase toward the ridge tip and no dacites are found at the ridge tip. Bar graphs showing the percentage of samples from 0.03-degree sections of the OSC axis that are (b) basaltic, (c) intermediate, and (d) high-silica in composition. In general, the number of high-silica samples decreases down axis, while the basaltic samples remains relatively constant or increases.

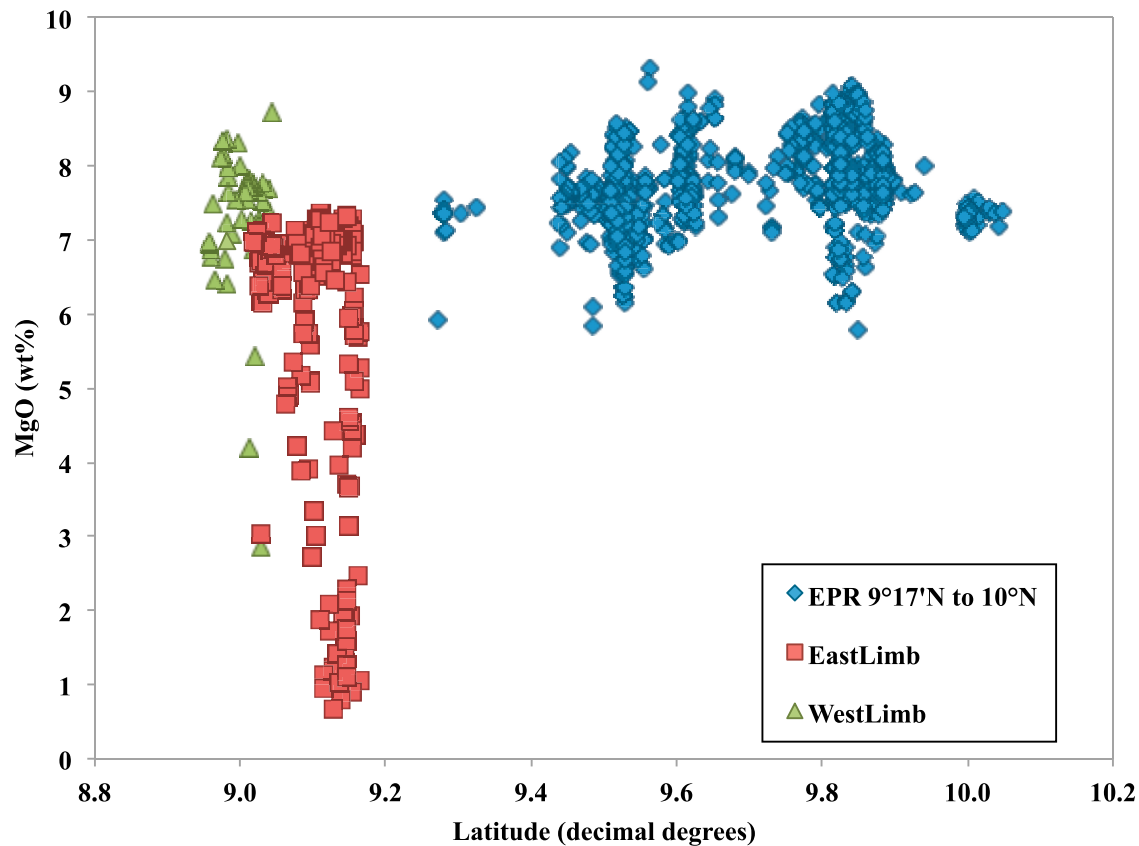


Figure 9. MgO (wt%) versus Latitude for lavas erupted on the northern EPR from the OSC to the Clipperton Transform Fault (8.8–10.2 decimal degrees). On average, the east limb OSC lavas are more evolved compared to typical northern EPR basalts. West limb lavas have an average MgO that is greater than east limb lavas.

LLD trends as well as those calculated using Petrolog [Danyushevsky and Plechov, 2011].

5.2. On-Axis Intermediate Lavas

[18] Intermediate compositions (basaltic andesites and andesites) erupted on-axis along the east limb of the OSC form from a combination of fractional crystallization and mixing of ferrobasalts and FeTi basalt melts with high-silica magmas (Figures 4 and 5). The most evolved compositions that formed solely from fractional crystallization are represented by ferroandesites with high-FeO concentrations (>12.5 wt%), while andesites with lower FeO have compositions consistent with magma mixing (Figure 4). Petrolog [Danyushevsky and Plechov, 2011] calculations suggest ~70 to 75% fractional crystallization (ol + plag + cpx and minor amounts of FeTi-oxide) of a N-MORB ferrobasaltic parent (265–43) at pressures of 1–2 kbar and 0.15 wt%

H₂O is required to explain the most evolved high-FeO andesite. However, fO_2 values must be no higher than QFM-1 to delay the onset of FeTi-oxide crystallization and produce the observed FeO and TiO₂ concentrations (Figures 4 and 5). Elevated P₂O₅ concentrations require that apatite fractionation has not occurred (Figure 5) during crystallization of these melts.

[19] Magma mixing is an important process in the formation of basaltic andesites and low-FeO andesites (<12.5 wt%). This is particularly apparent in compositional deviations of FeO, TiO₂, and P₂O₅ from values expected by simple fractionation of FeTi oxides and apatite at advanced stages of fractional crystallization. As shown in Figures 4 and 5, the basaltic andesites have elemental concentrations that fall along straight lines, consistent with mixing between high-silica magmas and a variety of evolved basaltic parent magmas. Linear trends observed in incompatible and compatible

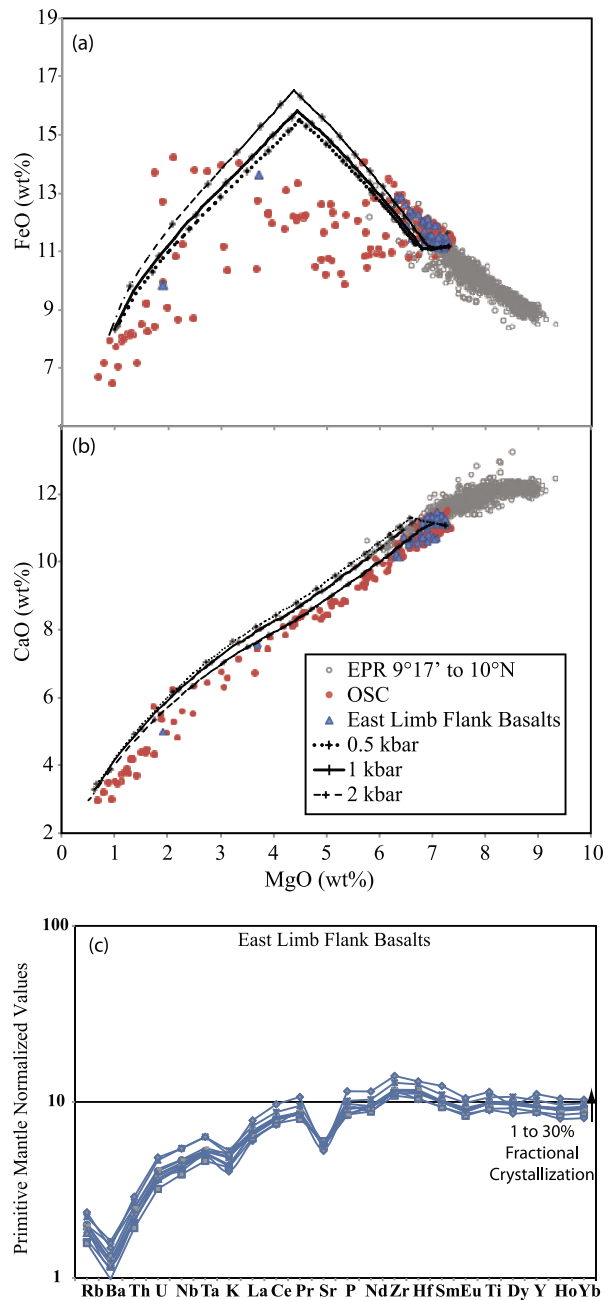


Figure 10. Geochemical diagrams showing the variation in basalts erupted in the east limb flank region compared to on-axis east limb OSC lavas (red filled circles) and northern EPR basalts (open gray circles). Major element diagrams include MgO versus (a) FeO and (b) CaO. East limb flank basalts can be produced by <30% fractional crystallization of the most mafic basalt from the region or by <50% crystallization of an EPR basalt with 8.5 wt% MgO. (c) Primitive mantle normalized diagram showing the variation in trace elements in east limb flank basalts.

trace element plots (i.e., Cr and Ni) versus Zr (Figure 7) also support this hypothesis. Assuming the lavas sampled were sourced from a sub-axial melt lens (or lenses), the wide range of axial lava compositions and variety of mixing trends indicate that the melt lens is not well mixed/homogeneous or, more likely, that a number of melt lenses exist over relatively short length (and time) scales that have had slightly different magmatic histories. Interestingly, there is no evidence of melts mixing with high-MgO magma compositions (Figures 4 and 5). Instead, all mixing lines trend toward moderately or highly evolved (<~7.5 wt.% MgO) basaltic compositions as the more mafic end-member. The apparent absence of a high-MgO end-member requires that a significant extent of magmatic fractionation must occur prior to mixing. It is likely that crystal fractionation occurs at variable levels in the lower to middle crust [e.g., *Natland and Dick, 2009*] but that significant crystallization also occurs within shallow melt lenses where the latent heat of crystallization provides the heat needed to assimilate preexisting crust and produce the silica-rich end-member melts [*Wanless et al., 2010*]. For more information on the where within the magmatic system crystallization occurs see auxiliary material.¹

5.3. East Limb Flank Lavas

[20] Although a wide range of lava compositions (basalts to dacites) were sampled from the east limb ridge axis at the OSC, samples recovered from the east limb flank (Figure 3) above the wide off-axis melt lens, have relatively restricted compositions. We refer to these lavas as “off-axis” although they are located between the two limbs of the OSC. Of the 63 lavas recovered from the flank region, 61 are ferrobasalts and FeTi basalts (the other two are andesites), with a limited range of major and trace element concentrations (Figure 10). These off-axis basalts are compositionally similar to basalts erupted on-axis and can be produced by <30% fractional crystallization from the most mafic east limb flank lava composition (7.29 wt% MgO) based on calculations using Petrolog (starting conditions; pressure = 1 kbar, $fO_2 = QFM$, $H_2O = 0.15$ wt%). None of the off-axis, east limb flank samples show evi-

¹Auxiliary materials are available in the HTML. doi:10.1029/2012GC004168.

dence indicative of mixing with high-silica lavas like those erupted on-axis (Figure 10).

6. Discussion

6.1. Distribution of Lava Compositions and Implications for Magma Supply at the OSC

[21] Lavas erupted at the east limb of the 9°N OSC vary systematically from south to north along the ridge axis, with compositions becoming more variable and on average more evolved with increasing distance from the ridge tip (Figures 3 and 8). This systematic variation is generally consistent with previous petrologic models of ridge propagation, suggesting an increase in magma supply away from the tip is sufficient to provide longer crustal residence times and therefore greater degrees of fractional crystallization [Christie and Sinton, 1981; Perfit *et al.*, 1983; Sinton *et al.*, 1983]. At the 9°N OSC, all lavas erupted within the ridge tip region (between ~8°58'N and 9°04'N) are moderately to highly evolved basalts (Figures 3 and 8). To the north, approximately 12 km behind the ridge tip (near 9°04'N), basaltic andesites are first observed. From this latitude northward, the degree of fractionation and variability in lava compositions increases until ~20 km behind the ridge tip (near 9°07'N), where the maximum petrologic variability is observed (ferrobasalts to dacites). The greatest range of lava compositions is observed from ~9°07'N to the northernmost edge of the study site ~9°10'N.

[22] In addition to these general trends in compositional variability, there are several important aspects of the 9°N lavas that provide insights into the thermal and magmatic conditions at the 9°N OSC. First, no high-MgO (>8 wt%) lavas were sampled anywhere along the east limb of the OSC (Figure 8), indicating crystallization/differentiation processes are efficient along the propagating ridge tip. Second, major and trace element compositions clearly indicate extensive magma mixing between high-silica melts and ferro- and FeTi basalts on-axis but not high-MgO lavas (Figures 4 and 5), suggesting that melts entering the shallow crust are evolved. This is consistent with several petrologic studies that indicate more primitive, higher temperature melts can undergo extensive fractionation during ascent through the lower crust prior to entering the melt lens [e.g., Natland and Dick, 2009; Wanless and Shaw, 2012] and is consistent

with some of the higher pressures of crystallization inferred for OSC lavas (see auxiliary material). Third, the highly evolved nature of the dacitic lavas from the northern portion of the east limb suggests that at times the magma supply rate to the upper crust (relative to the cooling rate) should be low or intermittent to allow for extensive crystallization prior to mixing with the ferro- and FeTi basalts. The fact that dacitic lavas were sampled on the axial graben floor and on the flanks of the graben wall indicates that conditions necessary for dacite petrogenesis have occurred repeatedly at the OSC. Finally, the formation of high-silica lavas requires that assimilation-fractional crystallization (AFC) processes were operative that necessitate unique tectonic and magmatic settings in which crustal temperatures, magma supply and magma budget allow for both extensive fractional crystallization and assimilation of seawater-altered crustal material [Perfit *et al.*, 1983, 1999; Wanless *et al.*, 2010, 2011].

[23] Overall the petrologic data suggest that crustal temperatures at the 9°N OSC can sustain melt bodies within the shallow crust on timescales that allow for relatively extensive but variable degrees of fractional crystallization, magma mixing, and in some instances, crustal assimilation to occur. In addition, the magmatic system must allow for both basalts and dacites to form at the ridge axis over relatively short times scales (both compositions were repeatedly collected from adjacent flows within the neovolcanic zone). We suggest that high-MgO basaltic magmas are supplied to the base of the crust beneath the propagating limb and that these melts undergo moderate degrees of differentiation during ascent and storage within the crust. Additionally, some melt may propagate from the wide melt lens down the ridge axis. However, intermittently, the melt supply (or flux in volume of melt through time) must decrease to the shallow melt lens, resulting in extensive fractional crystallization, and in some cases, crustal assimilation that may ultimately result in the formation of high-silica andesites and dacites.

6.2. Can the Geochemical and Geophysical Observations of Magma Supply at the OSC Be Reconciled?

[24] Understanding of the distribution of axial melt lenses has increased dramatically over the past few decades. However, variations in their spatial distribution and temporal longevity are not well constrained, principally because it is rare to have repeat

seismic surveys over the same section of the ridge axis. Here, we try to reconcile the current geophysical data with erupted lava compositions and petrologic constraints on magma evolution (described above), with the caveat that the present melt lens geometry may not have been the same in the past.

[25] Geophysical data from the 9°N OSC suggest relatively robust magma supply to the ridge discontinuity and include: (1) a narrow, but pronounced MLVZ the upper mantle directly below the east limb that widens to the south and extends between the two limbs of the OSC [Toomey *et al.*, 2007], (2) seismic evidence consistent with the presence of extensive melt within the shallow [Kent *et al.*, 2000] and mid- to lower crust [Bazin *et al.*, 2003] at the east limb of the OSC, and (3) relatively thick extrusive crust in the OSC basin and at the propagating tip of the east limb [Bazin *et al.*, 2001] but normal crustal thicknesses in the bathymetric track of the OSC off-axis [Canales *et al.*, 2003]. In contrast, the prevalence of intermediate and high-silica lavas suggest periods of relatively low (or at least intermittent) magma supply coupled with long crustal residence times that promote crystallization and mixing in the shallow crust. To understand the nature of magma supply to the OSC we must reconcile these seemingly contradictory geochemical and geophysical observations.

[26] The presence of a MLVZ is consistent with ~1–3% melt in the upper mantle about 9 km below the seafloor beneath the entire OSC [Toomey *et al.*, 2007]. Incompatible element ratios (e.g., La/Yb, Nb/Zr, and Ba/Zr) and isotopic compositions of the east limb OSC lavas are remarkably similar to N-MORB lavas erupted between 9°17' and 10°N on the EPR (Figure 6), indicating that similar melting conditions and source compositions are prevalent beneath both the east limb of the OSC and the EPR to the north. The absence of enriched MORB (E-MORB) in our east limb sample suite is consistent with the incompatible element depleted nature of the mantle beneath the east limb. Highly depleted incompatible element signatures (lower incompatible trace element ratios) indicative of enhanced mantle melting (and consequent increased magma supply) or unusually depleted sources (e.g., D-MORB from the Siqueiros Transform; [Perfit *et al.*, 1996]) beneath the OSC are also not observed. There is no indication from a geochemical viewpoint that the processes occurring in the mantle beneath the east limb are unusual. If normal extents of mantle melting (typical of the EPR to the north) have generated the parental magmas, then the presence of an anomalously wide melt lens [Kent

et al., 2000] and elevated extrusive crustal thicknesses observed at the OSC [Bazin *et al.*, 2001; Singh *et al.*, 2006] requires an explanation that does not include enhanced mantle melting. Similarly, although the range of lava compositions erupted at the OSC is likely related to an intermittent magma supply, the geochemical signatures cannot be related to variations in the extent of mantle melting.

[27] The presence of a wide melt lens extending off-axis and the eruption of andesites and dacites on-axis can be explained if melts formed in the mantle beneath the OSC accumulate over a wider region at the crust-mantle transition in response to shifting of magmatism from one axis to the other across the ridge discontinuity. This may result in the accumulation of melts in the lower crust or at the crust-mantle transition between the two limbs of the OSC. Vertical ascent of these melts through the crust between the two ridge axes results in the formation of the wide sill-like lens beneath and to the west of the east limb of the OSC. This melt can provide a source for the relatively young off-axis volcanism between the two limbs [Nunnery *et al.*, 2008; Waters, 2010] and the abundant volcanic edifices within the OSC basin [White *et al.*, 2009]. This distribution of melts over a wider region within the crust, may result in spatial and temporal fluctuations in magma supply to the shallow melt lens, allowing for the formation of high-silica lavas during periods of diminished melt delivery and mixing of diverse range of melt compositions.

[28] The extrusive layer (seismic layer 2A) at the east limb ridge tip and within the overlap basin is thicker than the average extrusive layer produced at the EPR [Bazin *et al.*, 2001]; however, the overall thickness of the crust produced at the OSC through time is similar to average EPR crust [Canales *et al.*, 2003]. Normal fast-spread crustal thickness is consistent with the geochemical evidence for normal extents of mantle melting. The increased thickness of volcanic crust within the overlap basin, however, may have formed from multiple eruptions in the overlap region due to the stagnant nature of the crust between the two opposing ridge limbs and the wide distribution of ephemeral melt bodies in the lowermost crust and mantle transition zone [Comber *et al.*, 2008; White *et al.*, 2009]. Therefore, we suggest that while magma supply to the melt lens may fluctuate over short timescales, the long-term supply to the region (including the east limb flank) is relatively normal.

6.3. Mid-Ocean Ridges and Steady State Magmatic Systems

[29] Crustal thicknesses produced along fast spreading ridges show little variation, which has led to the conclusion that the long-term magma supply to the ridge system is relatively constant or steady state [see *Perfit and Chadwick*, 1998, and references therein]. In addition, fast spreading ridges are thought to have steady state melt lenses that are quite stable in space and time. However, lavas erupted from sections of the EPR thought to have steady state melt lenses can have variable compositions suggesting differences in magma supply rates over 5 ka–1000 ka timescales [*Reynolds et al.*, 1992; *Perfit et al.*, 1994; *Regelous et al.*, 1999]. Thus, while the long-term supply to the crust might be steady state, short-term fluctuations in magma replenishment to the melt lens would account for the variability in lava compositions (even at “normal” ridge segments [e.g., *Batiza and Niu*, 1992]). Significant changes in lava composition have even been noted on decadal timescales at the few ridge locations where there have been repeat historic eruptions [e.g., *Embley et al.*, 2000; *Goss et al.*, 2010]. At the OSC, fluctuations in magma supply must occur over timescales long enough to account for the development of high-silica lavas but temporal constraints that would allow accurate estimates are lacking (see auxiliary material). High-silica lavas with similar compositions to those at the 9°N OSC recovered from the southern Juan de Fuca Ridge contain zircons that indicate differentiation from MORB parents over ~10–20 ka [*Schmitt et al.*, 2011]. Reconciling the geology of the OSC with magma supply is a function of both length-scale and time-scale of observation. To produce oceanic crust with “normal” thickness and basalt compositions magma supply at the OSC requires approximately steady state conditions but on shorter timescales, to generate the observed petrologic diversity, the magma supply must fluctuate.

7. Conclusions

[30] Extensive geophysical studies and detailed mapping and sampling of the 9°N OSC has resulted in the rare opportunity to directly compare the melt distribution within the crust to the composition of lavas erupted on the surface. Using the combination of major and trace element concentrations we show that the geophysical and geochemical observations at the 9°N OSC can be reconciled with a relatively normal, steady state magma supply from the mantle but non steady state magma supply to the upper

crust. Results of this study show that: (1) no high-MgO lavas (>8 wt% MgO) are erupted on the east limb of the OSC and all basaltic lavas are moderately evolved (ferro- to FeTi basalts), (2) the distribution of highly evolved andesites and dacites and moderately evolved basalts is generally consistent with previous petrologic models of ridge propagation, (3) fractional crystallization, crustal melting and extensive magma mixing are required to explain the compositions at the OSC, (4) despite a pronounced MLVZ, some thickened extrusive crust, and a wide melt lens, there is no evidence of enhanced extents of mantle melting beneath the region, (5) melt delivery to the crust is not restricted to the ridge axis and instead, is distributed over a wider region at the crust-mantle boundary, which can account for the wide, shallow melt lens, and (6) melt supply to the propagating ridge is intermittent over short timescales, which can reconcile many of the present geophysical interpretations with the petrologic observations at the 9°N OSC.

Acknowledgments

[31] We thank the Captain, officers and crew of the R/V *Atlantis* for all their help during cruise AT15-17 and the MEDUSA2007 Science party for their assistance in collecting data and samples for this study. We thank the Jason II shipboard and shore-based operations group for their help in collecting these data and HMR for processing all DSL-120 side scan and bathymetry collected during this cruise. Thanks to G. Kamenov and the UF Center for Isotope Geoscience for laboratory assistance. Thanks to J. Sinton and D. Toomey for the detailed reviews. R. Walters, M. Behn, A. Soule, and P. Canales provided insightful comments on earlier versions of the manuscript. This research was supported by the National Science Foundation (grants OCE-0527075 to MRP, OCE-0525872 to SMW, and OCE-0526120 to EMK).

References

- Barth, G. A., and J. C. Mutter (1996), Variability in oceanic crustal thicknesses and structure: Multichannel seismic reflection results from the northern East Pacific Rise, *J. Geophys. Res.*, *101*, 17,951–17,975, doi:10.1029/96JB00814.
- Batiza, R., and Y. Niu (1992), Petrology and magma chamber processes at the East Pacific Rise ~9°30'N, *J. Geophys. Res.*, *97*(B5), 6779–6797, doi:10.1029/92JB00172.
- Bazin, S., A. Harding, G. Kent, J. Orcutt, C. Tong, J. P. Ye, S. Singh, P. Barton, M. Sinha, and R. White (2001), Three-dimensional shallow crustal emplacement at the 9°03'N overlapping spreading center on the East Pacific Rise: Correlations between magnetization and tomographic images, *J. Geophys. Res.*, *106*(B8), 16,101–16,117, doi:10.1029/2001JB000371.
- Bazin, S., et al. (2003), A three-dimensional study of a crustal low velocity region beneath the 9°03'N overlapping

- spreading center, *Geophys. Res. Lett.*, *30*(2), 1039, doi:10.1029/2002GL015137.
- Canales, J., R. Detrick, D. Toomey, and W. Wilcock (2003), Segment-scale variations in the crustal structure of 150–300 kyr old fast spreading oceanic crust (East Pacific Rise, 8°15'N–10°5'N) from wide-angle seismic refraction profiles, *Geophys. J. Int.*, *152*, 766–794, doi:10.1046/j.1365-246X.2003.01885.x.
- Carbotte, S., and K. Macdonald (1992), East Pacific Rise 8°–10°30'N: Evolution of ridge segments and discontinuities from SeaMARC II and three-dimensional magnetic studies, *J. Geophys. Res.*, *97*(B5), 6959–6982, doi:10.1029/91JB03065.
- Carbotte, S., C. Small, and K. Donnelly (2004), The influence of ridge migration on the magmatic segmentation of mid-ocean ridges, *Nature*, *429*(6993), 743–746, doi:10.1038/nature02652.
- Christie, D., and J. M. Sinton (1981), Evolution of abyssal lavas along propagating segments of the Galapagos spreading center, *Earth Planet. Sci. Lett.*, *56*, 321–335, doi:10.1016/0012-821X(81)90137-0.
- Combiér, V., S. Singh, M. Cannat, and J. Escartin (2008), Mechanical decoupling and thermal structure at the East Pacific Rise axis 9°N: Constraints from axial magma chamber geometry and seafloor structures, *Earth Planet. Sci. Lett.*, *272*(1–2), 19–28, doi:10.1016/j.epsl.2008.03.046.
- Crawford, W. C., and S. C. Webb (2002), Variations in the distribution of magma in the lower crust and at the Moho beneath the East Pacific Rise at 9°–10°N, *Earth Planet. Sci. Lett.*, *203*(1), 117–130, doi:10.1016/S0012-821X(02)00831-2.
- Danyushevsky, L. V., and P. Plechov (2011), Petrolog3: Integrated software for modeling crystallization processes, *Geochem. Geophys. Geosyst.*, *12*, Q07021, doi:10.1029/2011GC003516.
- Detrick, R. S., P. Buhl, E. Vera, J. Mutter, J. Orcutt, J. Madsen, and T. Brocher (1987), Multi-channel seismic imaging of a crustal magma chamber along the East Pacific Rise, *Nature*, *326*(6108), 35–41, doi:10.1038/326035a0.
- Embley, R. W., W. W. Chadwick, M. R. Perfit, M. C. Smith, and J. R. Delaney (2000), Recent eruptions on the CoAxial segment of the Juan de Fuca Ridge: Implications for mid-ocean ridge accretion processes, *J. Geophys. Res.*, *105*, 16,501–16,525, doi:10.1029/2000JB900030.
- Ghiorso, M. S., and R. O. Sack (1995), Chemical mass transfer in magmatic processes IV. A revised and internally consistent thermodynamic model for the interpolation and extrapolation of liquid-solid equilibria in magmatic systems at elevated temperatures and pressures, *Contrib. Mineral. Petrol.*, *119*(2–3), 197–212, doi:10.1007/BF00307281.
- Goss, A. R., M. R. Perfit, W. I. Ridley, K. H. Rubin, G. D. Kamenov, S. A. Soule, A. Fundis, and D. J. Fornari (2010), Geochemistry of lavas from the 2005–2006 eruption at the East Pacific Rise, 9°46'N–9°56'N: Implications for ridge crest plumbing and decadal changes in magma chamber compositions, *Geochem. Geophys. Geosyst.*, *11*, Q05T09, doi:10.1029/2009GC002977.
- Harding, A., G. Kent, and J. Orcutt (1993), A multichannel seismic investigation of upper crustal structure at 9°N on the East Pacific Rise: Implications for crustal accretion, *J. Geophys. Res.*, *98*, 13,925–13,944, doi:10.1029/93JB00886.
- Haymon, R., D. Fornari, M. Edwards, S. Carbotte, D. Wright, and K. Macdonald (1991), Hydrothermal vent distribution along the East Pacific Rise crest (9°09'–54'N) and its relationship to magmatic and tectonic processes on fast-spreading mid-ocean ridges, *Earth Planet. Sci. Lett.*, *104*, 513–534, doi:10.1016/0012-821X(91)90226-8.
- Kamenov, G. D., M. R. Perfit, P. A. Mueller, and I. R. Jonasson (2008), Controls on magmatism in an island arc environment: Study of lavas and sub-arc xenoliths from the Tabar-Lihir-Tanga-Feni island chain, Papua New Guinea, *Contrib. Mineral. Petrol.*, *155*, 635–656, doi:10.1007/s00410-007-0262-0.
- Kent, G., A. Harding, and J. Orcutt (1993), Distribution of magma beneath the East Pacific Rise between the Clipperton transform and the 9°17'N Deval from forward modeling of common depth point data, *J. Geophys. Res.*, *98*, 13,945–13,969, doi:10.1029/93JB00705.
- Kent, G., S. Singh, A. Harding, M. Sinha, J. Orcutt, P. Barton, R. White, S. Bazin, R. Hobbs, and C. Tong (2000), Evidence from three-dimensional seismic reflectivity images for enhanced melt supply beneath mid-ocean-ridge discontinuities, *Nature*, *406*(6796), 614–618, doi:10.1038/35020543.
- Langmuir, C., J. Bender, and R. Batiza (1986), Petrological and tectonic segmentation of the East Pacific Rise, 5°30'–14°30'N, *Nature*, *322*(6078), 422–429, doi:10.1038/322422a0.
- Macdonald, K., and P. Fox (1983), Overlapping spreading centres: New accretion geometry on the East Pacific Rise, *Nature*, *302*, 55–58, doi:10.1038/302055a0.
- Macdonald, K., P. Fox, L. Perram, M. Eisen, R. Haymon, S. Miller, S. Carbotte, M. Cormier, and A. Shor (1988a), A new view of the mid-ocean ridge from the behaviour of ridge-axis discontinuities, *Nature*, *335*(6187), 217–225, doi:10.1038/335217a0.
- Macdonald, K., P. Fox, L. Perram, M. Eisen, R. Haymon, S. Miller, S. Carbotte, M. Cormier, and A. Shor (1988b), A new view of the mid-ocean ridge from the behaviour of ridge-axis discontinuities, *Nature*, *335*, 217–225, doi:10.1038/335217a0.
- Natland, J., and H. Dick (2009), Paired melt lenses at the East Pacific Rise and the pattern of melt flow through the gabbroic layer at a fast-spreading ridge, *Lithos*, *112*, 73–86, doi:10.1016/j.lithos.2009.06.017.
- Nunnery, A., E. M. Klein, M. Perfit, R. S. White, J. L. Mason, and A. J. Zaino (2008), Correlation of seafloor surface features and underlying melt bodies at the 9°N overlapping spreading center, East Pacific Rise, *Eos Trans. AGU*, *89*(53), Fall Meet. Suppl., Abstract V53D-03.
- Perfit, M. R., and W. W. Chadwick Jr. (1998), Magmatism at mid-ocean ridges: Constraints from volcanological and geochemical investigations, in *Faulting and Magmatism at Mid-Ocean Ridges*, *Geophys. Monogr. Ser.*, vol. 106, edited by W. R. Buck et al., pp. 59–115, AGU, Washington, D. C., doi:10.1029/GM106p0059.
- Perfit, M., and D. Fornari (1983), Geochemical studies of abyssal lavas recovered by DSRV Alvin from Eastern Galapagos Rift, Inca Transform, and Ecuador Rift: 2. Phase chemistry and crystallization history, *J. Geophys. Res.*, *88*, 10,530–10,550, doi:10.1029/JB088iB12p10530.
- Perfit, M. R., D. J. Fornari, A. Malahoff, and R. Embley (1983), Geochemical studies of abyssal lavas recovered by DSRV Alvin from Eastern Galapagos Rift, Inca Transform, and Ecuador Rift: 3. Trace element abundances and petrogenesis, *J. Geophys. Res.*, *88*, 10,551–10,572, doi:10.1029/JB088iB12p10551.
- Perfit, M., D. Fornari, M. Smith, J. Bender, C. Langmuir, and R. Haymon (1994), Small-scale spatial and temporal variations in mid-ocean ridge crest magmatic processes, *Geology*, *22*(4), 375–379, doi:10.1130/0091-7613(1994)022<0375:SSSATV>2.3.CO;2.
- Perfit, M., et al. (1996), Recent volcanism in the Siqueiros transform fault: Picritic basalts and implications for MORB

- magma genesis, *Earth Planet. Sci. Lett.*, *141*, 91–108, doi:10.1016/0012-821X(96)00052-0.
- Perfit, M. R., W. I. Ridley, and I. R. Jonasson (1999), Geologic, petrologic and geochemical relationships between magmatism and massive sulfide mineralization along the eastern Galapagos Spreading Center, *Rev. Econ. Geol.*, *8*, 75–99.
- Perfit, M., V. D. Wanless, W. I. Ridley, E. Klein, M. Smith, A. Goss, J. Hinds, S. Kutza, and D. Fornari (2012), Lava geochemistry as a probe into crustal formation at the East Pacific Rise, *Oceanography*, *25*(1), 89–93, doi:10.5670/oceanog.2012.06.
- Regelous, M., Y. Niu, J. I. Wendt, R. Batiza, A. Greig, and K. D. Collerson (1999), Variations in the geochemistry of magmatism on the East Pacific Rise at 10°30'N since 800 ka, *Earth Planet. Sci. Lett.*, *168*, 45–63, doi:10.1016/S0012-821X(99)00048-5.
- Reynolds, J. R. (1995), Segment-scale systematics of mid-ocean ridge magmatism and geochemistry, PhD thesis, 483 pp., Columbia Univ., Palisades, N. Y.
- Reynolds, J. R., C. H. Langmuir, J. F. Bender, K. A. Kastens, and W. B. F. Ryan (1992), Spatial and temporal variability in the geochemistry of basalts from the East Pacific Rise, *Nature*, *359*, 493–499, doi:10.1038/359493a0.
- Rubin, K., and J. Sinton (2007), Inferences on mid-ocean ridge thermal and magmatic structure from MORB compositions, *Earth Planet. Sci. Lett.*, *260*(1–2), 257–276, doi:10.1016/j.epsl.2007.05.035.
- Schmitt, A., M. R. Perfit, K. H. Rubin, D. F. Stockli, M. C. Smith, L. A. Cotsonika, G. F. Zellmer, W. I. Ridley, and O. M. Lovera (2011), Rapid cooling rates at an active mid-ocean ridge from zircon thermochronology, *Earth Planet. Sci. Lett.*, *302*, 349–358.
- Sempere, J., and K. Macdonald (1986), Deep-tow studies of the overlapping spreading centers at 9°03'N on the East Pacific Rise, *Tectonics*, *5*(6), 881–900, doi:10.1029/TC005i006p00881.
- Singh, S., A. Harding, G. Kent, M. Sinha, V. Comber, S. Bazin, C. Tong, J. Pye, P. Barton, and R. Hobbs (2006), Seismic reflection images of the Moho underlying melt sills at the East Pacific Rise, *Nature*, *442*(7100), 287–290, doi:10.1038/nature04939.
- Sinton, J., D. Wilson, D. Christie, R. Hey, and J. Delaney (1983), Petrologic consequences of rift propagation on oceanic spreading ridges, *Earth Planet. Sci. Lett.*, *62*, 193–207, doi:10.1016/0012-821X(83)90083-3.
- Sinton, J. M., S. M. Smaglik, J. J. Mahoney, and K. C. Macdonald (1991), Magmatic processes at superfast spreading mid-ocean ridges: Glass compositional variations along the East Pacific Rise 13–23°S, *J. Geophys. Res.*, *96*, 6133–6155, doi:10.1029/90JB02454.
- Smith, M., M. Perfit, and I. Jonasson (1994), Petrology and geochemistry of basalts from the southern Juan de Fuca Ridge: Controls on the spatial and temporal evolution of mid-ocean ridge basalt, *J. Geophys. Res.*, *99*, 4787–4812, doi:10.1029/93JB02158.
- Smith, M., M. Perfit, D. Fornari, W. Ridley, M. Edwards, G. Kurras, and K. Von Damm (2001), Magmatic processes and segmentation at a fast spreading mid-ocean ridge: Detailed investigation of an axial discontinuity on the East Pacific Rise crest at 9°37'N, *Geochem. Geophys. Geosyst.*, *2*(10), 1040, doi:10.1029/2000GC000134.
- Stakes, D., M. Perfit, M. Tivey, D. Caress, T. Ramirez, and N. Maher (2006), The Cleft revealed: Geologic, magnetic, and morphologic evidence for construction of upper oceanic crust along the southern Juan de Fuca Ridge, *Geochem. Geophys. Geosyst.*, *7*, Q04003, doi:10.1029/2005GC001038.
- Tong, C., J. Pye, P. Barton, R. White, M. Sinha, S. Singh, R. Hobbs, S. Bazin, A. Harding, and G. Kent (2002), Asymmetric melt sills and upper crustal construction beneath overlapping ridge segments: Implications for the development of melt sills and ridge crests, *Geology*, *30*(1), 83–86, doi:10.1130/0091-7613(2002)030<0083:AMSAUC>2.0.CO;2.
- Toomey, D., D. Joussetin, R. Dunn, W. Wilcock, and R. Detrick (2007), Skew of mantle upwelling beneath the East Pacific Rise governs segmentation, *Nature*, *446*(7134), 409–414, doi:10.1038/nature05679.
- Wanless, V. D., and A. M. Shaw (2012), Lower crustal crystallization and melt evolution at mid-ocean ridges, *Nat. Geosci.*, *5*, 651–655, doi:10.1038/ngeo1552.
- Wanless, V. D., M. R. Perfit, W. I. Ridley, and E. Klein (2010), Dacite petrogenesis on mid-ocean ridges: Evidence for oceanic crustal melting and assimilation, *J. Petrol.*, *51*(12), 2377–2410, doi:10.1093/petrology/egq056.
- Wanless, V. D., M. R. Perfit, W. I. Ridley, P. J. Wallace, C. B. Grimes, and E. M. Klein (2011), Volatile abundances and oxygen isotopes in basaltic to dacitic lavas on mid-ocean ridges: The role of assimilation at spreading centers, *Chem. Geol.*, *287*(1–2), 54–65, doi:10.1016/j.chemgeo.2011.05.017.
- Waters, C. L. (2010), Temporal and petrogenetic constraints on volcanic accretionary processes at 9–10°N East Pacific Rise, PhD thesis, 261 pp., Mass. Inst. of Technol.–Woods Hole Oceanogr. Inst. Jt. Program in Oceanogr./Appl. Ocean Sci. and Eng., Cambridge, Mass.
- White, S., R. Haymon, D. Fornari, M. Perfit, and K. Macdonald (2002), Correlation between volcanic and tectonic segmentation of fast-spreading ridges: Evidence from volcanic structures and lava flow morphology on the East Pacific Rise at 9°–10°N, *J. Geophys. Res.*, *107*(B8), 2173, doi:10.1029/2001JB000571.
- White, S. M., J. L. Mason, K. C. Macdonald, M. R. Perfit, V. D. Wanless, and E. M. Klein (2009), Significance of widespread low effusion rate eruptions over the past two million years for delivery of magma to the overlapping spreading centers at 9°N East Pacific Rise, *Earth Planet. Sci. Lett.*, *280*(1–4), 175–184, doi:10.1016/j.epsl.2009.01.030.